Geophysical Journal International

Geophys. J. Int. (2014) **199,** 1187–1204 doi: 10.1093/gji/ggu322

GJI Mineral physics, rheology, heat flow and volcanology

The Eyjafjallajökull volcanic system, Iceland: insights from electromagnetic measurements

Marion P. Miensopust,[1,2,*] Alan G. Jones,[1] Gylfi Páll Hersir[3] and Arnar M. Vilhjálmsson[3]

[1] *Dublin Institute for Advanced Studies, School of Cosmic Physics, Dublin, Ireland. E-mail: Marion.Miensopust@liag-hannover.de*
[2] *Institut für Geophysik, Westfälische Wilhelms-Universität Münster, Germany*
[3] *Iceland GeoSurvey, Reykjavík, Iceland*

Accepted 2014 August 20. Received 2014 August 19; in original form 2014 January 15

SUMMARY

Electromagnetic (EM) measurements were performed 1 yr after the most recent eruption of the Eyjafjallajökull volcano (2010 March–May), southern Iceland, to investigate the geometries of structures of the volcano system through imaging lateral and vertical electrical resistivity variations. High quality magnetotelluric (MT) and transient EM data were acquired at 26 sites around Eyjafjallajökull and the southern part of Mýrdalsjökull (the glacier covering the Katla volcano). For some locations the steep topography has influence on the MT responses, but this can be compensated by static shift correction using the transient EM data and/or including topography in the modelling mesh. As expected, qualitative indicators, such as phase tensor ellipses and induction arrows, infer a concentration of conductive material beneath Eyjafjallajökull. 2-D resistivity models are presented from data along three profiles: Along the river valley of Markarfljót in the north, along the coast to the south of Eyjafjallajökull and across the mountain ridge Fimmvörðuháls between Eyjafjallajökull and Katla. In numerous previous studies elsewhere in Iceland a conductive layer at about 10–30 km depth was identified. From our data, such a conductor is also present in the northeastern part of the investigated area. Additionally, all profiles show a conductive, near-surface layer at about 1–2 km depth, as seen previously for example at the Hengill geothermal region. A connection between those two conductive layers is indicated by the resistivity models, and the dyke (flank eruption) and the conduit (summit eruption) appear as vertical conductive structures. It is uncertain if the vertical connection is permanent or a transient feature as consequence of the eruptive sequences. Subsequent measurements are required when the volcano system is quiescent.

Key words: Geomagnetic induction; Magnetotellurics; Remote sensing of volcanoes.

1 INTRODUCTION

Iceland has numerous active volcanoes, some of which are covered by glaciers. Of these, Katla in southern Iceland is a large system and one of the most active in Iceland, with at least 20 eruptions within the central volcano and one in its fissure swarm during the past 1100 yr (Larsen 2000; Elíasson *et al.* 2006). The last eruption in 1918 is almost 100 yr ago, hence the heightened concern. The volcano is mostly covered by the Mýrdalsjökull ice cap and accordingly eruptions within the Katla volcano are phreato-magmatic in type and are capable of producing jökulhlaups, that is sudden glacial outburst floods (Sturkell *et al.* 2010). The neighbouring volcano, 25 km to the west, is Eyjafjallajökull, which is covered by a smaller and thinner glacier. It is less active than Katla, with the most recent eruption in 2010 March/April and four other recorded eruptions since settlement of the area some 1000 yr ago. The last two historic events both occurred in tandem with Katla eruptions, the first simultaneously with the Katla eruption of 1612, and the second being the eruption in 1821–1823 that was immediately followed by an eruption of Katla (Sturkell *et al.* 2010, and references therein). Both volcanoes are in proximity to populated areas and to international flight paths, which makes them both highly potent societal threats, although the eruption volumes of Katla has been significantly larger than for Eyjafjallajökull and hence Katla is far more significant in terms of potential societal effects and threats. The recent eruptive events of the Eyjafjallajökull volcano have focused major public concern and interest—more so than ever before—on volcanic eruptions, not only on their local effects but

*Now at: Leibniz Institute for Applied Geophysics (LIAG), Hannover, Germany.

also on potential long-distant effects on daily life. Scientific interest is overwhelming in gaining as much information as possible about the volcanic structures and processes to enhance understanding of underlying processes.

For a while, it was uncertain if the jökulhlaup (i.e. glacier-outburst flood) that occurred on 2011 July 9 east of the town of Vík was a result of a small eruption at Katla volcano under the Mýrdalsjökull ice cap or if it was related to geothermal activity. Recent geochemical work by Galeczka *et al.* (2014) strongly suggests that the heat source for the glacier melting was geothermal in nature rather than volcanic. Nevertheless, ongoing continuous seismic activity suggests that there is magma movement beneath Katla volcano and an eruption is still to come. Therefore, interest in knowing the volcanic structures of both volcanoes, and particularly in enhancing our understanding of the possible links between them, is heightened.

Beside numerous petrological and geochemical studies, reports of geophysical investigations on the Eyjafjallajökull and Katla volcanoes have been published over the last two to three decades, including results from GPS measurements (e.g. Árnadóttir *et al.* 2008), earthquake studies (e.g. Dahm & Brandsdóttir 1987; Einarsson & Brandsdóttir 2000), radar altimetry and interferometry (e.g. Gudmundsson *et al.* 2007; Hooper *et al.* 2009), seismic surveys (e.g. Gudmundsson *et al.* 1994) and aeromagnetic measurements (e.g. Jónsson & Kristjánsson 2000). The bedrock surface of Mýrdalsjökull has been mapped by radio echo soundings (Björnsson *et al.* 2000). Sigmundsson *et al.* (2010) outline their understanding of the intrusive processes based on GPS measurements, interferometric analysis of satellite radar images and seismic data recorded over several months before and during the 2010 eruptive events. However, prior to the pilot study presented here, conducted by the Dublin Institute for Advanced Studies and the Iceland GeoSurvey, no electric or electromagnetic (EM) data have been acquired with the objective to image the resistivity structure beneath and around these two volcanoes. This is an obvious paucity, as EM methods are far more sensitive to fluid distribution (in this case partial melt) than any other geophysical method. Therefore, the aim of our study was to investigate the resistivity structure beneath and around the Eyjafjallajökull using magnetotelluric (MT) and transient EM (TEM) methods, and to draw conclusions about fluid pathways and their interconnectivity from the resulting electrical resistivity models.

2 EM METHODS

In recent years, geophysical methods involving EM induction techniques have undergone significant progress because of the improved quality of observations, data processing, analysis and modelling, and interpretation gained from new technological advances and increased computational power, respectively (see, e.g. Chave & Jones 2012). Electrical conductivity is related to the rock petrophysical properties and the amount, connectivity and type of fluid within the rocks, including the presence of melts (or partial melts; e.g. Shankland 1975; Stegena 1976; Schwarz 1990; Jödicke 1992; Selway 2014), but it is also strongly enhanced by the presence of metallic conductors (e.g. graphite, sulphide and iron oxides). Diffusion of EM fields into the subsurface is a function of the square root of the period (i.e. 1/frequency), ranging from a few metres for the highest frequencies (hundreds of kHz, so-called radio-MT, RMT) to hundreds of kilometres (so-called long period MT, LMT) for the longest periods (thousands to tens of thousands of seconds). This wide depth range, together with the vast range of electrical conductivity in natural rocks (several orders of magnitude), is the reason why EM methods are applicable for studying a broad range of problems (e.g. Ferguson *et al.* 2012). Although geophysical methods investigating the resistivity structure of the subsurface have great potential for imaging magma chambers and, therefore, for enhancing the knowledge and understanding of volcanic systems, application of such methods is surprisingly still not a standard tool in volcanic research, with the exception of geothermal energy potential studies (e.g. Jones & Dumas 1993; Árnason *et al.* 2010; Bertrand *et al.* 2013). Recently, MT measurements were applied to the active andesite cone volcano Mount Ruapehu in New Zealand (Ingham *et al.* 2009) and showed a low resistivity dyke-like feature that is most likely the volcanic feeder system that also supplies the other volcanoes of the Tongariro Volcanic Centre and marks the conduit by which hot gases and (occasionally) magma reach the surface. The summit vent of the Mount Ruapehu volcano, is occupied by a crater lake, whereas the Icelandic volcanoes Katla and Eyjafjallajökull calderas are ice-capped. Nevertheless the results of Ingham *et al.* (2009) and also of Hill *et al.* (2009) who investigated the melt distribution of Mount St Helens and Mount Adams in the State of Washington, USA, strongly imply that the objective of using EM methods—especially MT—to determine the resistivity structure and thereby enhancing the knowledge and understanding of the volcanic structure is realistic and obtainable. MT is an established EM method in both academia and commercial applications, and measures the time variation of the natural electric and magnetic field (e.g. Chave & Jones 2012). MT is a natural source, deep probing EM method that is used to determine the resistivity structure of the subsurface and, therefore, provides useful information that helps to improve the understanding of complex structures and the tectonic evolution of a region (e.g. Jones & Craven 1990; Davis *et al.* 2003; Evans *et al.* 2005; Spratt *et al.* 2009; Miensopust *et al.* 2011). In Iceland, MT has a long but sporadic history; it has been applied to geothermal targets for over three decades (e.g. Hermance & Grillot 1974; Árnason *et al.* 2010; Hersir *et al.* 2013) and to address the nature of the mantle plume (e.g. Kreutzmann *et al.* 2004), but oddly not to investigate volcanic systems per se in detail (for a review of MT in Iceland see Björnsson *et al.* 2005). These days, MT in Iceland is mainly applied to geothermal areas and is usually combined with TEM soundings to correct for static shifts in the MT data (e.g. Árnason *et al.* 2010; Hersir *et al.* 2013).

3 GEOLOGICAL AND TECTONIC SETTING

Iceland is part of the oceanic lithosphere and the island sits astride the Mid Atlantic Ridge from southwest to northeast (see Fig. 1 for geological map). Along the ridge an active spreading axis appears as a zone of active rifting and volcanism (e.g. Flóvenz & Sæmundsson 1993). The divergent plate boundary between North America and Eurasia has a relative motion of approximately 18–20 mm yr^{-1} in a direction of 102–104° E of N (DeMets *et al.* 1994; Sella *et al.* 2002). Estimates of the crustal thickness of Iceland varies from 8 to 15 km (above an anomalous mantle) with shallowest depths beneath the volcanic rift zone (e.g. Flóvenz & Sæmundsson 1993) of 15–46 km (e.g. Menke 1999; Allen *et al.* 2002; Fedorova *et al.* 2005). The highly inhomogeneous upper crust is characterized by sequences of flood basalts and hyaloclastites and consequently by variable near-surface *P*-wave velocities (e.g. Pálmason 1971; Flóvenz 1980; Flóvenz &

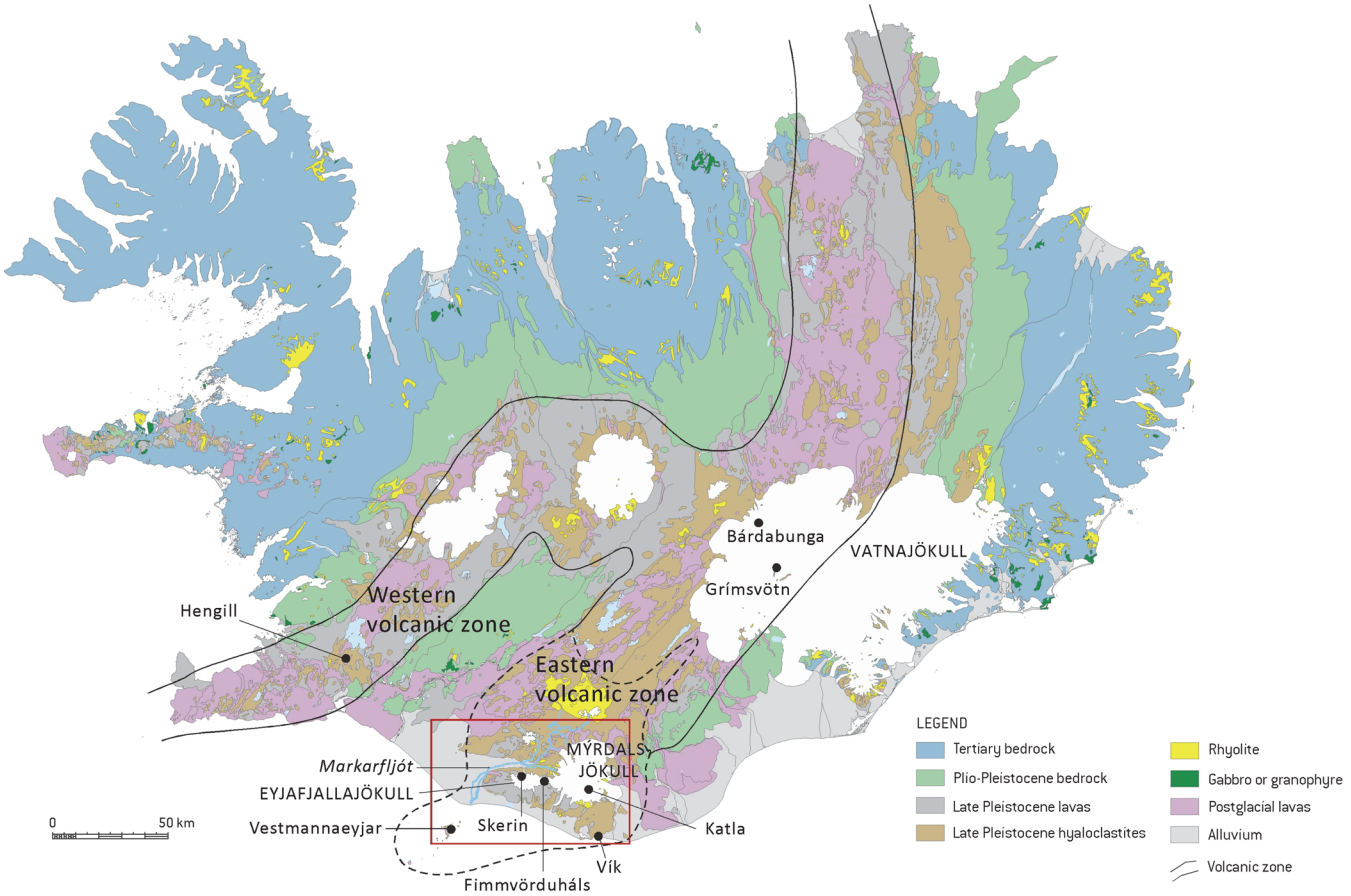

Figure 1. Geological map of Iceland and important localities (simplified from Jóhannesson & Saemundsson 1999).

Gunnarsson 1991; Kaban *et al.* 2002). In the mid- to lower-crustal depth range of 10–35 km velocities are reported as being in the range of 7.0–7.4 km s^{-1} (Båth 1960; Pálmason 1971; Bjarnason *et al.* 1993; White *et al.* 1996; Brandsdóttir *et al.* 1997; Darbyshire *et al.* 1998). Based on different interpretations of seismic data with and without the support of MT, heat flow and/or gravity data, this layer was subject to the debate about two very different and competing models: a thin and hot crust model (Pálmason 1971; Beblo & Björnsson 1978, 1980; Gebrande *et al.* 1980; Flóvenz & Sæmundsson 1993) and a thick crust model (Båth 1960; Pavlenkova & Zverev 1981; Bjarnason *et al.* 1993; Menke & Levin 1994; White *et al.* 1996; Darbyshire *et al.* 1998, 2000a,b; Weir *et al.* 2001). The interpretation of this layer as subsolidus crustal material (e.g. Pavlenkova & Zverev 1981; Menke & Levin 1994) supports the current prevailing belief in the thick crust model.

A transform fault system in southern Iceland, the South Iceland Seismic Zone (SISZ), separates two subparallel rift zones, the Western Volcanic Zone and the Eastern Volcanic Zone (Darbyshire *et al.* 2000b) and rifting presently is being transferred from the Western Volcanic Zone to the Eastern Volcanic Zone (EVZ; Jóhannesson 1980). The EVZ is a propagating rift outside the main zone of plate spreading in Iceland (Sigmundsson *et al.* 2010) with a spreading rate decreasing from the northeast (15 mm yr^{-1}) to the southwest (9 mm yr^{-1}; Schreiber-Enslin *et al.* 2011). The EVZ extends from Bárdarbunga and Grímsvötn volcanoes within the Vatnajökull ice cap in the northeast to the Vestmannaeyjar central volcano in the southwest (*cf.* Fig. 1). The rifting structure (fissure swarms and hyaloclastite ridges) dominate the rifting activities in the EVZ north of the junction with the SISZ and therefore, the northern part is called Eastern Volcanic Rift Zone. In contrast, the part south of the junction is dominated by little spreading and large central volcanoes, and is called Eastern Volcanic Flank Zone. Eyjafjallajökull is a central volcano located at the southern termination of the EVZ. It is 27 km long (E–W) with a maximum width of 14 km (N–S) and covers an area of about 300 km^2 (Fig. 2). The maximum elevation (on the southern rim of the summit caldera) is 1651 m a.s.l. and above ∼1000 m it is covered by a small (about 80 km^2) glacier extending 14–15 km in E–W direction (Larsen *et al.* 2012). The thickness of the ice cover was 200–250 m in the summit caldera and less than 100 m outside the caldera prior to the 2010 eruption (Strachan 2001; Gudmundsson *et al.* 2005). Katla is a central volcano about 25 km to the east of Eyjafjallajökull. Its maximum elevation is 1512 m a.s.l. and it is covered by the Mýrdalsjökull glacier except at nunataks along the caldera rim. The diameter of the caldera is about 10 km and it is covered with 200–700-m-thick ice.

3.1 Crustal conductors

Previous MT work in Iceland dating back to the late-1970s and early-1980s (e.g. Beblo & Björnsson 1978, 1980; Hersir *et al.* 1984; Eysteinsson & Hermance 1985) repeatedly showed a conductor at about 10–12 km depth nearly everywhere beneath Iceland. The conductive layer was initially interpreted to be due to partial melt (10–20 per cent, e.g. Hersir *et al.* 1984) in the crust (at 1100–1200 °C) and is still believed to be connected to melt, at least below some parts of the island. However, strong arguments against the

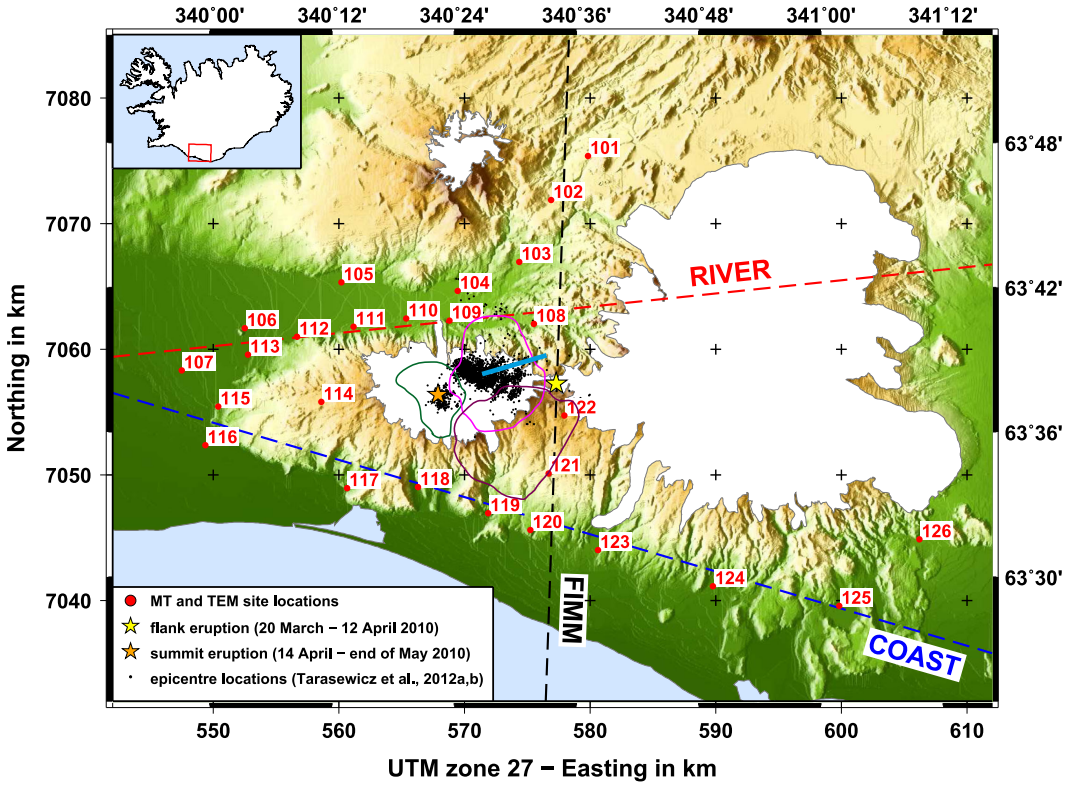

Figure 2. Map showing the locations of the 26 MT and TEM sites as well as the flank and summit eruption sites. Coloured dashed lines indicate the three profiles COAST (blue), FIMM (black) and RIVER (red). The black dots are earthquake locations by Tarasewicz *et al.* (2012a,b). The coloured lines outline sill and dyke structures after Sigmundsson *et al.* (2010, purple – 'sill 1', pink – 'sill 2', green – 'contracting sill', turquoise – dyke). The white areas denote glacial coverage.

presence of a considerable amount of partial melt at this depth interval have been put forward based on a study of the attenuation of seismic waves by Menke *et al.* (1995); later Kaban *et al.* (2002) also concluded that considerable melt within the lower crust of Iceland is unlikely. In a recent interpretation of resistivity data from the high temperature area Hengill, SW Iceland, it is proposed that the deep conductors might reflect dikes and magma intrusions and the conductive layer could be due to magmatic brines trapped in ductile intrusive rocks (Árnason *et al.* 2010).

Recently, Spichak *et al.* (2013) presented a new conceptual model of the Icelandic crust in the Hengill geothermal area based on the so-called 'indirect EM geothermometry' whose validity still needs to be proven. They postulate a two-layer background temperature of up to 200 °C for the top 5–7 km and varying temperature between 200 and 400 °C beneath down to a depth of about 20 km. This background temperature model of supposedly gabbro composition is consistent with the model of a relatively thick and cold crust. Furthermore, they presume a network of interconnected high-temperature channels overlying the background temperature. Based on the laboratory studies by Duojun *et al.* (2002, Spichak *et al.* (2013) conclude that the observed high conductivity layers in the middle-lower crust cannot be formed by gabbro and, therefore, the high-temperature, low-resistivity channels could be partly molten basalt. They assume that the molten basalt is upwelling from the depth of the mantle through faults and fractures and rises to the rheologically weakened layer at 10–15 km depths, where it spreads laterally. Hot magma also is thought to penetrate into the permeable upper crustal layers, where it does not form a continuous high-temperature, low-resistivity layer but rather cools down within shallow local pockets at 1.5–2.5 km, which are according to Spichak *et al.* (2013) often connected with the underlying high-temperature layer by conduits.

3.2 Eyjafjallajökull eruptions

There are five known eruptions of Eyjafjallajökull since settlement started in Iceland. In the 10th century (around 920), a radial fissure eruption occurred and formed the 4.5 km long and approximately 100-m-wide Skerin ridge, which extends to the WNW from the summit caldera of the Eyjafjallajökull volcano and is partially covered by ice (Oskarsson *et al.* 2010). The multicompositional Skerin ridge was produced by a single eruption of mildly alkaline lava and tephra of silicic and mafic composition. From the characteristics of the Skerin products, Oskarsson *et al.* (2010) concluded that dynamic magma mixing took place shortly prior to and during the eruption, and that the eruption involved intrusion and mixing of basaltic magma with a silicic magma body sitting high within the volcano. In 1612/13, Eyjafjallajökull erupted again, but very little is known about this small summit eruption. The last eruption of Eyjafjallajökull before the 2010 events was an extended event lasting 14 months from 1821 December to 1823 January. This summit eruption had a short phreato-magmatic phase in 1821 December which was followed by a year-long period of intermittent magmatic/phreato-magmatic activity and flooding (Larsen *et al.* 1999; Sigmundsson *et al.* 2010).

In 2010, two eruptions preceded each other very quickly. From 2010 March 20 to April 12 an effusive flank eruption of basalt took place at Fimmvörðuháls (a few kilometres east of the summit caldera). On 2010 April 14 an explosive summit eruption of

trachyandesite began. The sequences of activity of the intrusion processes triggering the explosive eruption, based on GPS, interferometric satellite radar (InSAR) and seismic data obtained prior to and during the eruptions, and can be summarized after Hjaltadóttir & Vogfjörd (2010) and Sigmundsson *et al.* (2010) as follows. Since measurements began there were over 20 yr of quiescence before a long series of intermittent magmatic events were observed starting in 1992. In 1994 and 1999, inflation and seismicity were interpreted as extensive sill intrusions at 4.5–6.5 km and of volumes of $\sim$10–17 $\times$ 10^6 m^3 and $\sim$21–31 $\times$ 10^6 m^3, respectively (Sturkell *et al.* 2003; Pedersen & Sigmundsson 2004, 2006; Hooper 2008; Hooper *et al.* 2009; Sigmundsson *et al.* 2010; Sturkell *et al.* 2010). From mid-2000 to 2009 seismicity was observed intermittently and surface deformation was negligible. In mid-2009, a seismic episode lasting a few weeks associated with related deformation (with 10–20 mm of southward displacement on the south side of the volcano) occurred. Around the year change 2009/2010 deformation, as well as seismicity, increased again with earthquake clusters approximately east of the summit that subsequently migrated towards the SSE. Sigmundsson *et al.* (2010) explain their crustal displacement observations by a single horizontal sill (purple line in Fig. 2) inflating at a depth of 4.0–5.9 km under the southeastern flank of the volcano, which is in good agreement with the locations of the earthquake foci. They explain the March pre-eruptive deformation by a second sill (pink line Fig. 2) beneath the northeastern flank of the volcano, together with a southeast-tilted dyke (turquoise line in Fig. 2) reaching from 3.2–6.1 km depth to few hundred metres or less below surface. At the same time a dramatic rise in intensity of seismic events is observed, where the foci form a E–W trending segment east of the main cluster, with basically no seismicity in the southeastern area. Seismicity started to ascend towards the surface beneath the ice-cap on 2010 March 17, but three days later seismicity and hence the magma took a turn in the uppermost 2–3 km towards the ice-free Fimmvörðuháls mountain pass, where late in the evening of the 2010 March 20 the first eruption started (Gudmundsson *et al.* 2012a). This eruption produced in total $\sim$20 $\times$ 10^6 m^3 of basaltic lava (Edwards *et al.* 2012). During the 3-week-long flank eruption most of the seismicity originated from the area of the bend in the magma pipe, whereas the deformation almost ceased when the vent opened and the volcano remained in an inflated stage without significant subsidence until 2010 April 9. The petrology of the olivine-basalt magma produced by the flank eruption infers that it is of deep origin and had a short crustal residence time above 13 km (Keiding & Sigmarsson 2012). The flank eruption ended on 12 April.

On 14 April the explosive eruption phase began when a new set of vents formed at the ice-capped summit of the volcano (Sigmundsson *et al.* 2010). Seismic activity at 10–12 km depth just south of the summit crater preceded the eruption coincident with magma still making its way towards the surface at Fimmvörðuháls (Hjaltadóttir & Vogfjörd 2010). Hjaltadóttir *et al.* (2012) describe the development of seismic activity as follows: On 13 April, the area became more active at 7 km depth and, after a M_L 2.3 event, an intense seismic swarm occurred lasting over 2.5 hr that was concentrated in two clusters (i.e. 5.5–7.5 km and 0.5–3 km). On 14 April a third cluster formed at 10–11 km depth and a continuous tremor signal at 1 Hz indicated that magma had emerged on the surface beneath the ice cap. The gap in seismic activity between 3 and 5.5 km is interpreted as a small magma chamber. In the same depth range is a horizontal deflating sill (green line in Fig. 2) modelled by Sigmundsson *et al.* (2010). The tephra from 14 to 19 April consists of three types of magma (i.e. basaltic, intermediate and silicic composition), indicating rapid magma mingling of evolved FeTi-basalt with silicic melt that is identical in composition to the 1821–1823 summit eruption (Sigmarsson *et al.* 2011; Gudmundsson *et al.* 2012b). The summit eruption is characterized by four consecutive and distinct phases (Gudmundsson *et al.* 2012a): an inital/first explosive phase (14–18 April); a low discharge and mixed effusive explosive phase (18 April–4 May); a second explosive phase (5–17 May); and a final phase of declining activity(18–22 May). Only a few, shallow earthquakes were detected during the first two phases, but in sharp contrast during the third phase several earthquakes at 18–23 km depth indicated the recharging of the system with new magma from the mantle (Hjaltadóttir & Vogfjörd 2010). The deep-root magma recharge is supported by compositional changes in the tephra after 5 May (Sigmarsson *et al.* 2010). The summit eruption ended in late 2010 May and produced in total a dense rock equivalent volume of $\sim$180 $\times$ $10^6$$m^3$ erupted material (Gudmundsson *et al.* 2012b).

4 DATA COLLECTION AND PROCESSING

4.1 Field campaign 2011 July

In 2011 July, broad-band MT (BBMT) data were collected at 26 sites around the Eyjafjallajökull and the southern part of Mýrdalsjökull (see Fig. 2 for site locations). The site distribution and areal layout are unfortunately not ideal to investigate the structures beneath and around the volcano as intended, but were as good as possible. Setting up an equi-spaced array is logistically impractical, as many areas are hardly accessible, and some not at all, and steep slopes hinder system installation. Furthermore, the glacial caps of Eyjafjallajökull and Katla (i.e. Mýrdalsjökull) and the nearby coastline preclude more measurements to the south and east of the volcano as well as on top of it using standard land-MT equipment. Therefore, the resulting site distribution is more profile-based than a regular 2-D array.

The BBMT sites used Phoenix Geophysics equipment, namely MTU-5A recording boxes and MTC-50 induction coils, and recorded time-series data for approximately 40 hr at most sites and at a far distant remote reference site about 150 km away during the whole survey. The obtained period range of good quality data is approximately 0.003 s to 1000–2000 s. At each of the BBMT sites, the two horizontal, perpendicular magnetic field components H_x and H_y were recorded, as well as the vertical magnetic field component H_z (except for site 105). The two horizontal, perpendicular electric field components E_x and E_y were measured using non-polarizing Pb–PbCl (lead–lead chloride) electrodes (PE4 electrodes from Phoenix Geophysics) laid out in a cross with a dipole length of typically 100 m. In addition, at each MT site (except for site 116) central loop transient EM (TEM) data were obtained primarily for static shift control of the MT data. The TEM data were recorded with a PROTEM 20-channel system from Geonics Limited at 25 Hz using a transmitter loop of 200 m$\times$ 200 m and a 1 m^2 receiver loop with 100 windings (i.e. effective area of 100 m^2).

4.2 MT data processing

Phoenix commercial remote-reference processing software [based on Jones & Jödicke (1984)/method 6 in Jones *et al.* (1989), which

uses Least Trimmed Squares (Rousseeuw 1984; Rousseeuw & Leroy 1987) with Cook's Distance (Cook 1977) to minimise variance] was used to process the time-series of the MT data into frequency domain MT transfer functions. One reference site about 150 km distance away from the array at the Eyjafjallajökull was available for remote-reference processing. Nevertheless, to obtain the best response curves also all available sites that recorded simultaneously were investigated as remote sites for each other. Furthermore, both magnetic field and electric field references were considered, not only magnetic field references as is the norm in MT. For many sites electric field remote reference resulted in superior estimates of the response curve for short periods, whereas magnetic field remote reference produced superior results for long periods. Therefore, for each site individually the best combination of far and local remote sites and electric and magnetic field reference was merged to obtain the MT transfer functions. Fig. 3 displays typical response estimates; the apparent resistivity and phase curves, as well as induction arrows using the Wiese convention (Wiese 1962, real arrows plot away from current concentrations), for an example site (EYJ108). In this case, the transfer function displayed is one where merging of different references did not improved the estimates, and therefore the whole curve was obtained using the same reference. In general, data quality is very good and the transfer functions suggest at least for the first three decades (i.e. a few hundred Hz to a few seconds) a 1-D structure (i.e. very small induction arrows and identical shape of the XY and YX resistivity curves and phase curves that lie on top of each other).

4.3 Phase tensor

Small-scale, near-surface resistivity heterogeneities and topography can seriously affect MT responses (Jones 2012). This phenomenon is known as galvanic distortion (for more details see Section 4.4). If the distortion is such that it only affects the electric field and not the magnetic field (as assumed for the MT case), the phase relationship between the horizontal electric and magnetic field vectors will be unaffected and only the amplitudes of the observed electric field are distorted. Taking advantage of this, Caldwell *et al.* (2004) introduced the phase tensor approach that has the advantage that the phase tensor is immune to electric field galvanic distortion effects. One intuitive graphical representation of the phase tensor is as an ellipse. The principle axes of the phase tensor ellipse ($\phi_{\max}$, $\phi_{\min}$) indicate the horizontal directions of the maximum and minimum induction current, which reflects lateral variations in the resistivity structure. The phase tensor skew angle (β), and the variation of the direction of the major axis of the phase tensor ellipse, can help in determining the dimensionality of the structure. In the case of an isotropic, 1-D structure, $\phi_{\max} = \phi_{\min}$ and therefore the phase tensor will be represented by a circle. In the 2-D case, $\phi_{\max} \neq \phi_{\min}$ and the phase tensor is represented by an ellipse. For the 1-D and 2-D cases, the phase tensor is symmetric (theoretically: $\beta = 0$), whereas for the 3-D case the phase tensor is not symmetric and accordingly the skew angle will be non-zero. Fig. 4 shows phase tensor maps, including induction arrows, for 0.5, 1.5 and 7.5 km depth below surface (Niblett-Bostick penetration depth estimation). This is an unusual presentation of the phase tensor; typically the phase tensors are plotted at particular frequencies/periods. However, this introduces a huge visual misrepresentation in cases where there is significant lateral variation in electrical resistivity (e.g. Hamilton *et al.* 2006; Miensopust *et al.* 2011). The colour of the phase tensor ellipses represents the skew angle β (left-hand side) and $\phi_{\min}$ (right-hand side), respectively. At 0.5 and 1.5 km depths (Fig. 4) the phase tensor ellipses are almost all nearly circular and therefore indicate 1-D resistivity structures at shallow depth (conforms with the statement above regarding the first three decades of the response curves and Fig. 3). At 7.5 km depth most phase tensor ellipses are elongated indicating a more complex structure than 1-D. The skew angles β are relatively small for all depths and the induction arrow lengths are very short, both indicators for low dimensionality. Large $\phi_{\min}$ values at 0.5 km depth indicate an overall increasing conductivity with depth for the whole survey area. At 1.5 km depth the sites close to the eruption locations show moderate $\phi_{\min}$ values (i.e. indicative of a less strong decrease in resistivity), whereas all other sites still require a strong decrease in resistivity. At greater depth (7.5 km), the $\phi_{\min}$ values suggest rather constant resistivities or a slight increase. At shallow depths the real induction arrows (red; Wiese convention) point away from the Eyjafjallajökull indicating a more conductive structure there compared to the surrounding areas. At greater depths almost all real induction arrows point away from the Atlantic Ocean. The Icelandic continental shelf has a shallow bathymetry (<100 m) for the first few kilometres off the coast line, therefore the coast effect only affects long periods/greater depths (see also Fig. 3).

4.4 Static shift correction

Distortion comprises all the small-scale, near-surface conductivity inhomogeneities that cannot be resolved within the conductivity model of the subsurface, but still affect the MT responses, that is distort them (e.g. Berdichevsky *et al.* 1973; Jiracek 1990; Jones 2012). The complex process of distortion can be separated into galvanic and inductive effects (Berdichevsky *et al.* 1973). For the MT case the quasi-static approximation ($\sigma = \varepsilon/T$) is assumed and therefore, the inductive part of distortion can be ignored (Berdichevsky & Dmitriev 1976a,b). The galvanic effect is caused by primary electric fields that produce electrical charges where conductivity gradients occur, that is at distinct boundaries or at continuous transitions. The total electric field is distorted because the excess charges result in secondary electric fields that add vectorially to the primary field. The effects of galvanic distortion on the magnetic field is usually neglected for MT, as its influence vanishes for low frequencies (e.g. Chave & Jones 1997; Garcia & Jones 2002). The galvanic electric field effectively channels the current into conductive inhomogeneities and around resistive inhomogeneities (e.g. Smith 1997). Jiracek (1990) showed that these galvanic effects are not only produced by resistive or conductive inclusions but also by topography that can cause the so-called galvanic topographic effect. The topographic galvanic effect occurs when the primary electric field is perpendicular to the trend of the topography. There are no surface charges at the top of a hill nor at the bottom of a valley; the maximum charge concentration can be found where the topography is steepest. Unlike the 'normal' galvanic distortion effects, the galvanic topographic effects do not require a conductivity inhomogeneity to be present.

The simplest case of galvanic distortion is an upward or downward shift that is asymptotically a constant—or static—shift of the MT log–log apparent resistivity versus period curve. Therefore these effects are known as *static shifts* (Jones 1988). If available, TEM data can be used to correct for static shifts in MT responses, either by joint inversion allowing vertical shifts in the MT apparent resistivity curves or by using a correction scheme that is based on the TEM soundings (e.g. Sternberg *et al.* 1988; Pellerin & Hohmann 1990; Sternberg 1993; Árnason *et al.* 2010). One approach is to convert the TEM sounding into a pseudo-MT response directly

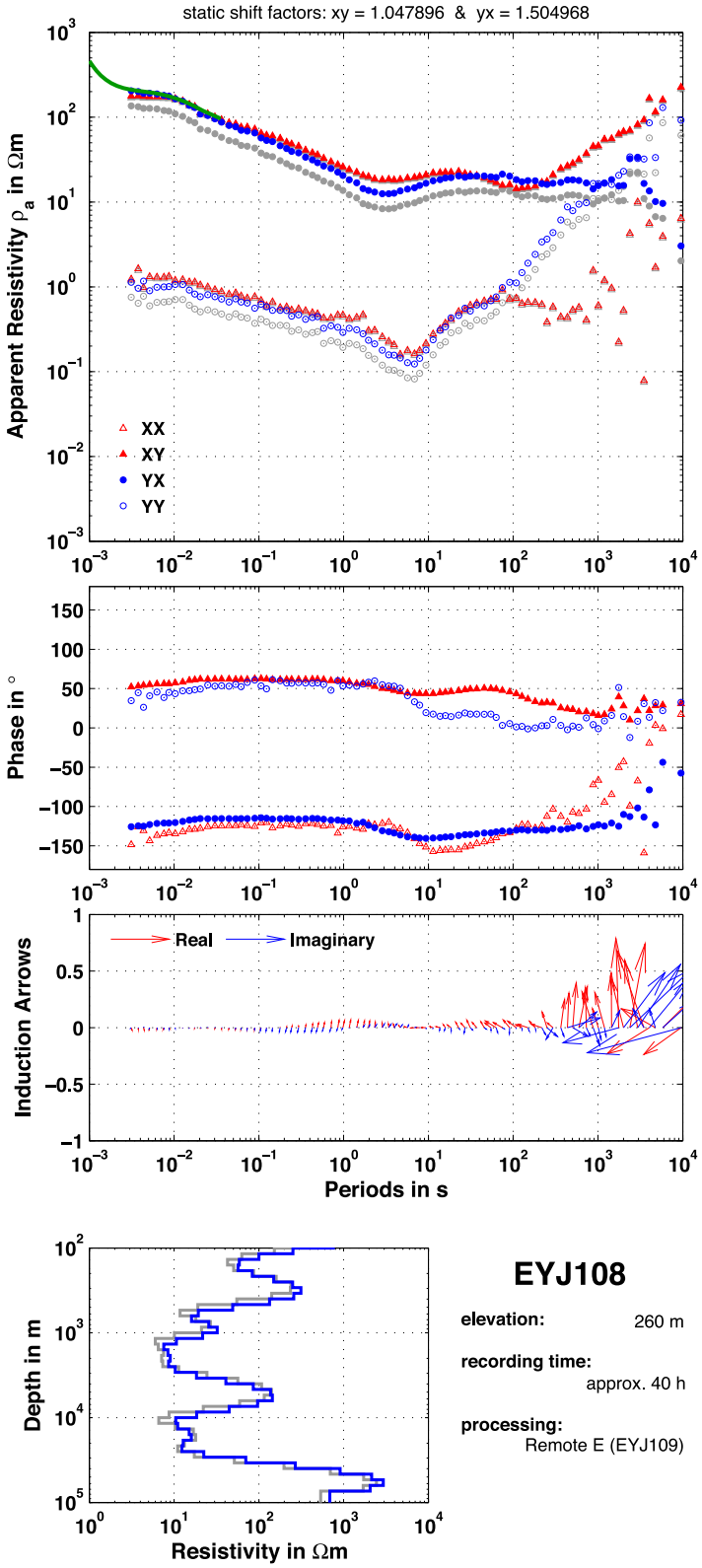

Figure 3. Response curves of an example site. Apparent resistivity curves (top), phase curves (middle) and induction arrows in Wiese convention (Wiese 1962) are shown. The grey symbols represent the original resistivity data whereas the coloured symbols are the data corrected by the static shift factors specified above based on the TEM data, which is represented by the green line (see Section 4.4). Below are information of this particular site and the obtained 1-D Occam models (grey – using original data; blue – using static shift corrected data) of the invariants (see Section 5.1).

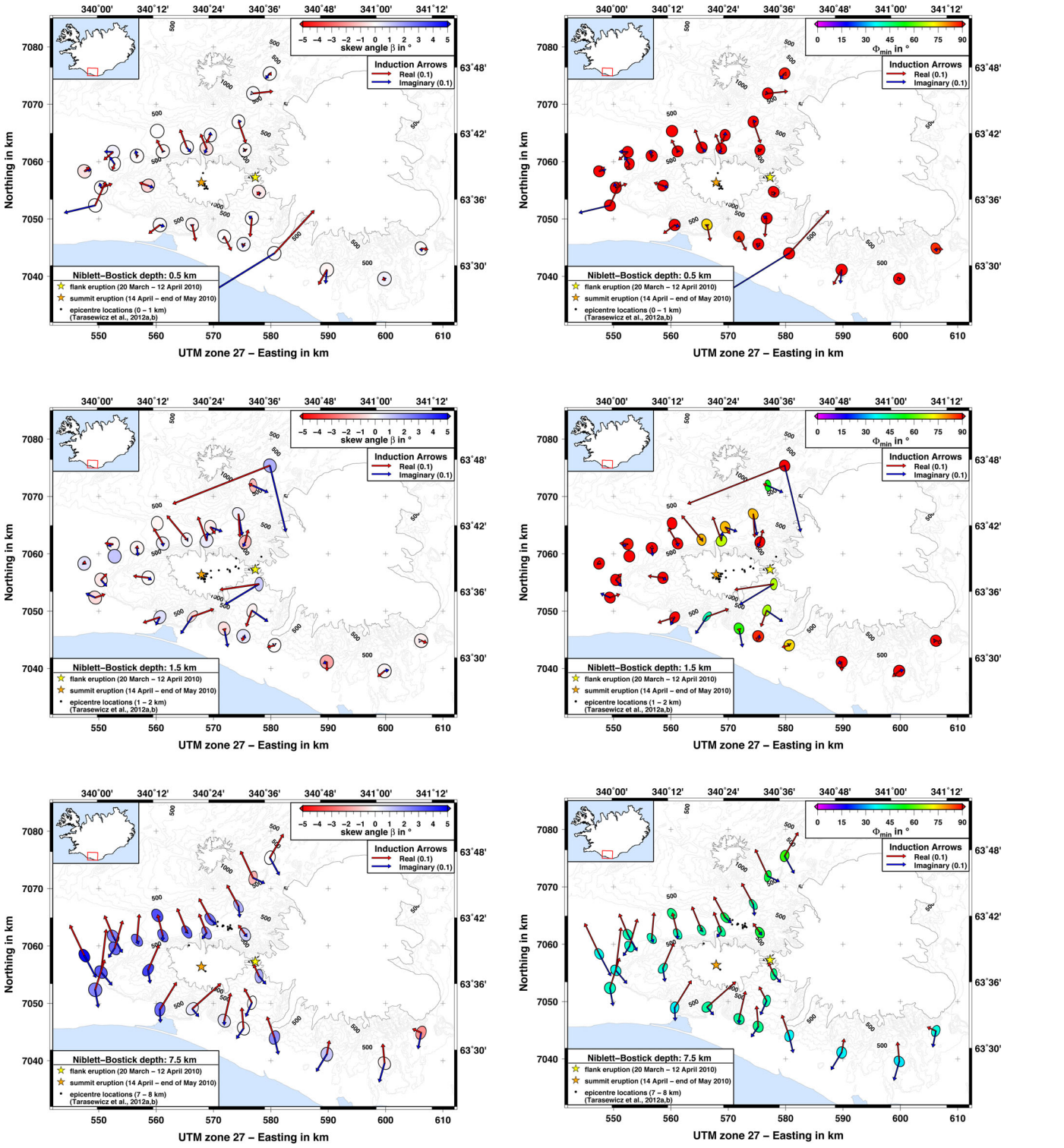

Figure 4. Maps of phase tensor ellipses and induction arrows. For three different depths (0.5, 1.5 and 7.5 km) the real (red) and imaginary (blue) induction arrows are plotted using the Wiese convention (Wiese 1962). The arrow length in the legend represents a value of 0.1. The colour of the phase tensor ellipses (axes normalized by $\phi_{\max}$) indicate (left-hand side) the skew angle β and (right-hand side) $\phi_{\min}$, respectively. (Note: the comparable large induction arrow estimates at some sites are not reliable values as the induction arrows for those sites and period range, that is in the MT dead-band, scatter a lot.) The black dots are earthquake locations by Tarasewicz *et al.* (2012a,b).

using a simple time-shift or alternatively via 1-D inversion of the TEM data followed by MT forward modelling of the obtained model. These strategies are only accurate if the overlapping region between MT and TEM is 1-D, but for multidimensional environments the approach might at least provide a useful indication of a static shift problem.

The additionally collected TEM data at all sites (except for site 116) allows us to apply such a static shift correction approach to the

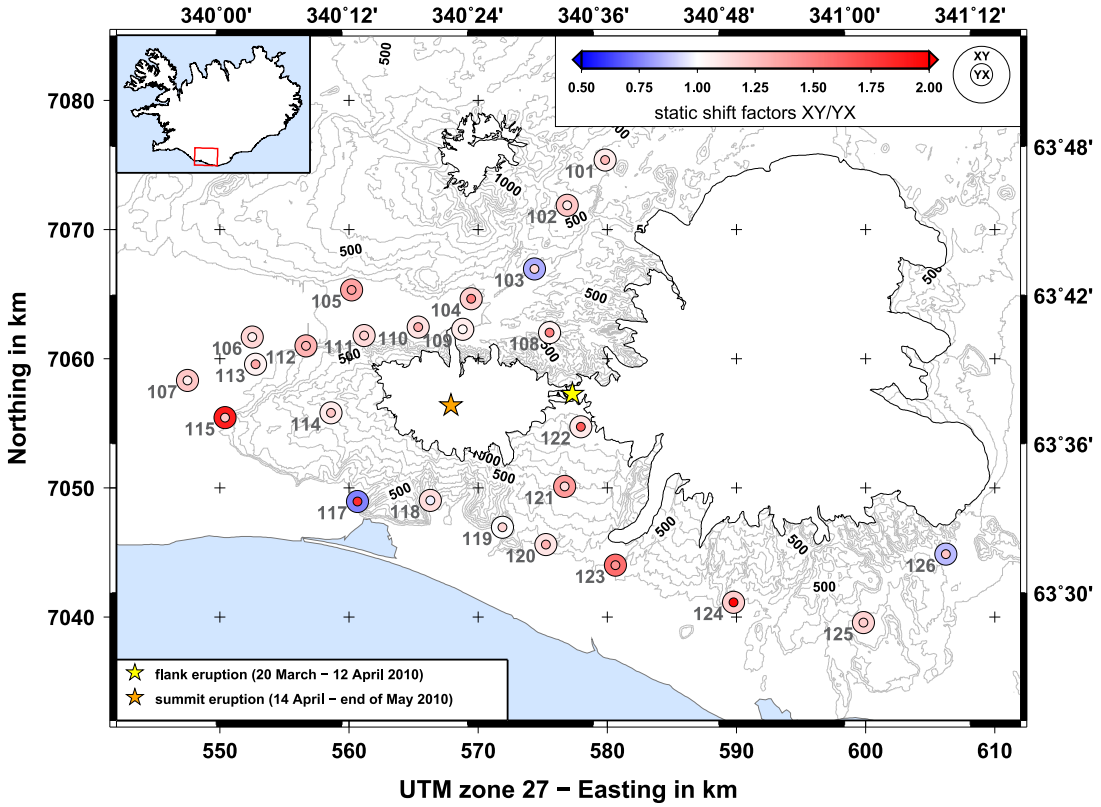

Figure 5. Map showing the static shift parameters XY and YX for all sites that have MT and TEM data (i.e. site 116 is missing). The outer circle represents the XY shift factor and the inner dot the YX shift factor. The topography is indicated by the grey contour lines and the outlines of the glaciers are shown as well.

MT data. Usually MT data are displayed against the log(periods) (T_{MT}) in seconds, whereas the TEM data are commonly plotted against time (t_{TEM}) in milliseconds. Sternberg *et al.* (1988) empirically found a simple time-shift to be applied to the TEM data to convert them into a pseudo-MT response:

$$T_{\mathrm{MT}}(\text{in s}) = \frac{t_{\mathrm{TEM}}(\text{in ms})}{200} = \frac{t_{\mathrm{TEM}}(\text{in s})}{0.2}. \quad (1)$$

As an example site, the converted TEM sounding using eq. (1) is shown as pseudo-MT resistivity curve in Fig. 3 (solid green line). The static shift factors specified in Fig. 3 are obtained by calculating the mode (i.e. most frequent value) of the differences in resistivity between the TEM data and each of the XY and YX components of the MT data (grey symbols). The shift factor XY is applied to the top row of the MT impedance tensor, that is the XX and XY MT data, and the YX factor to the bottom row, the YX and YY components; this is because the static effect on Ex will affect both XX and XY impedance components, whereas the static shift effect on Ey will affect YX and YY impedance components. The corrected MT data are represented by the coloured symbols. Fig. 5 shows a map of all XY and YX static shift factors obtained. Most sites show negligible static shift effects, whereas a few have more significant effects (mainly only on one E-field direction). Three sites (103, 117, 126—*cf.* and/or Fig. 5 for locations) show a shift factor >1 for one direction and <1 for the other direction. These three sites are all located in valleys. The sites that have a static shift factor close to 2 for one direction are all close to a steep slope (sites 115, 124). In those cases, the shift factor is large for the total electric field that is perpendicular to the trend of the topography (note, for XY the electric field is directed N–S, whereas for YX it is E–W). Therefore, the static shift effects found are considered to some extent topography driven (see Jiracek 1990).

5 INVERSION

5.1 1-D models

The above analyses suggests that a 1-D approach is valid to obtain an initial impression of the near-surface resistivity structures. Therefore, the Berdichevsky invariant of the MT impedance elements, that is geometric mean of resistivities ϱ_{xy} and ϱ_{yx} and arithmetic mean of phases ϕ_{xy} and ϕ_{yx}, were used to calculate 1-D Occam models (Constable *et al.* 1987). The inversion was run for maximum of 10 iterations using 45 layers with depth limits set to 100 m (top) and 100 km (bottom). Fig. 3(bottom) shows the 1-D Occam resistivity-depth profile obtained for the example site. Such resistivity-depth profiles were calculated for all sites and most exhibit (as in Fig. 3) two conductive layers—one at about 1–3 km depth and the other one at about 10 km depth below surface. Fig. 6 shows pseudo-2-D depth-sections of the three profiles COAST (along the coast), FIMM (across mountain ridge at Fimmvörðuháls) and RIVER (in river valley of Markarfljót) (see Fig. 2 for locations) along which the individual 1-D Occam models were smoothly gridded (see figure caption for details). These depth-sections show the presence of the shallow conductor nearly everywhere and, in some parts, a dominant second conductor below 10 km. Note for profile COAST sites 115 and 116 project onto nearly identical positions, and preference has been given to the model for site 115 as 116 did not have any TEM data for static shift correction. Also site 113 is not included in profile RIVER as it projects onto a nearly identical

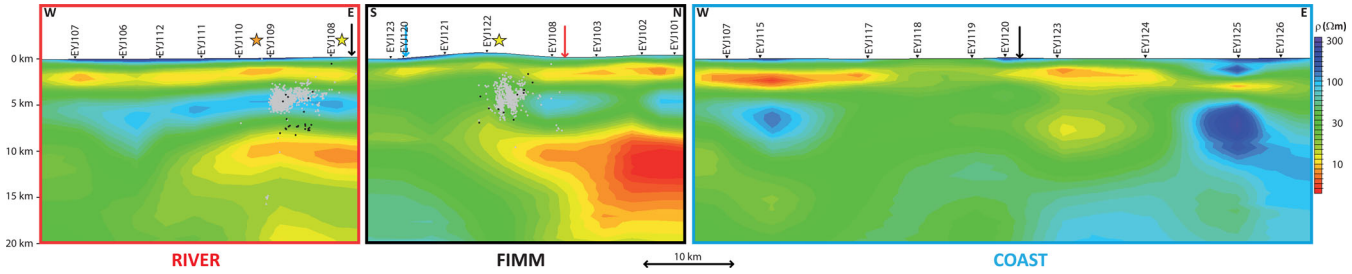

Figure 6. Depth-sections of the three profiles COAST, FIMM and RIVER. Depth-sections are gridded (interpolation radius 3, spline weight 0, smoothing factor 4) Occam 1-D models of the Berdichevski invariants for each site. The coloured box around each depth-section indicates where the profile is located (dashed line of same colour in Fig. 2) and intersections with other profiles are indicated by an arrow of the same colour. The yellow and orange stars mark the locations (projected onto the profile) of the flank and summit eruptions, respectively. The black (≤2 km distance to profile) and grey (2–5 km distance to profile) dots are the projected earthquake locations by Tarasewicz *et al.* (2012a,b).

position as 106, but only recorded for a very short time (it was damaged by Icelandic horses after 5.5 hr).

5.2 2-D models

For each profile the MT data were decomposed and regional 2-D MT respones were generated, using the distortion decomposition code by McNeice & Jones (2001); based on the Groom-Bailey decomposition (Bailey & Groom 1987; Groom 1988; Groom & Bailey 1989), with respect to each profile direction (i.e. COAST = 106° E of N, FIMM = 2° E of N, RIVER = 84° E of N). Where necessary, a D^+ consistency assessment (Parker 1980, 1982) was applied to these data to eliminate inconsistent data points prior to inversion.

One should keep the assumptions made for 2-D modelling and inversion in mind. For 2-D models, resistivity varies with depth and along the profile but is assumed to be constant perpendicular to the profile (i.e. parallel to strike direction). In the ideal 2-D case, electric and magnetic fields are orthogonal to each other, which allows decoupling into two independent modes. One mode, which describes the currents flowing parallel to the strike direction, is called the transverse electric (TE) mode. The other mode, which describes the currents flowing perpendicular to strike direction, is known as the transverse magnetic (TM) mode. The XY′ and YX′ components derived in the geoelectric strike coordinates represent essentially the two modes: TE and TM, respectively.

Due to the diverse profile directions the associated TE and TM modes corresponded to very different geographical directions. Furthermore, a data rotation by 90°causes a mode flip when assigning TE and TM modes to the XY′ and YX′ components. This is the case for FIMM, as the strike direction is 92°. For the shallow part, where the subsurface is essentially 1-D, the resulting models will hardly be affected by incorrect mode assignment. At longer periods (i.e. greater depth), where 3-D structures are present, the models are potentially subject to artefacts due to mode flip. A number of authors have already investigated the problems and limitations of using 2-D approaches, when modelling and inverting 3-D data and described potential problems with artefacts especially introduced by the TE mode data (e.g. de Lugão & Kriegshäuser 1997; Garcia *et al.* 1999; Ledo *et al.* 2002; Ledo 2005). For some geometries, the TM mode data are more affected (e.g. Hermance 1982; Park & Mackie 1997), but in the majority of cases it is the TE mode data that are primarily affected as those data do not include any effects due to charges.

The 2-D finite difference, smooth model inversion code used (Mackie 2002; Baba *et al.* 2006, based on Rodi & Mackie 2001) offers the choice between a standard Laplacian regularization (i.e. using the actual model mesh to compute the Laplacian) and a uniform grid Laplacian regularization (i.e. using a uniform model mesh). Furthermore, minimization of the gradient or the Laplacian can be selected to calculate the models. A Tikhonov regularization parameter τ controls the trade-off between fitting the data and the model smoothness. A larger τ results in smoother models at the expense of higher rms misfits. Therefore, initial inversion runs for all three profiles were necessary to determine the optimal regularization parameter for the chosen mesh and data. A 100 Ωm homogeneous half-space starting model and all data (error floors of 5 per cent for resistivities, 3.5 per cent for phases (∼1°) and 0.03 for tipper) were used for those tests varying τ in the range of 0.1–100. All four combinations of regularization and minimization were considered and accordingly L-curves were plotted. Based on the L-curves, a $\tau = 3$ and uniform grid Laplacian regularization with minimization of gradient were considered as optimum parameter setting for all three profiles. Using those settings, each profile was inverted introducing the different data (TE and TM mode resistivity and phase and tipper) iteratively. The initial error floors of resistivities were 50 per cent, of the phases 50 per cent and 1.0 for the tipper. They were successively reduced to 5 per cent for resistivities (ρ), 3.5 per cent for phases (ϕ) and 0.03 for tipper. Three different orders to include the data were tested:

(i) $\phi_{TM} \rightarrow$ add $\phi_{TE} \rightarrow$ add $\rho_{TM} \rightarrow$ add $\rho_{TE} \rightarrow$ add tipper
(ii) $\phi_{TM} \rightarrow$ add $\phi_{TE} \rightarrow$ add tipper $\rightarrow$ add $\rho_{TM} \rightarrow$ add ρ_{TE}
(iii) tipper $\rightarrow$ add $\phi_{TM} \rightarrow$ add $\phi_{TE} \rightarrow$ add $\rho_{TM} \rightarrow$ add ρ_{TE}.

Furthermore, meshes with and without topography were used and the original as well as the static shift corrected MT data were used for inversion. The final rms values of all inversion runs are of the same order (RIVER: 1.1–1.3, FIMM: 2.8–3.0, COAST: 1.3–1.9) and do not allow selection or rejection of any of those models. In general, all those resulting 2-D models are relatively consistent with each other in each set regarding the major resistivity structures; nevertheless there are differences in some parts of the models. As an example all 12 inversion results are shown for profile RIVER in Fig. 7. The overall rms values for each model is stated at the bottom right-hand corner of each plot, and site-by-site rms values are plotted below. Projected earthquake locations after Tarasewicz *et al.* (2012a,b) are shown as black (less than 2 km from profile) and grey (2–5 km away) dots. Niblett–Bostick penetration depth estimations indicate that the TE and TM mode data at all sites cover at least the depth range shown in the models.

The top left-hand model (no topography, no static shift correction, order i) shows significantly different resistivity structures at

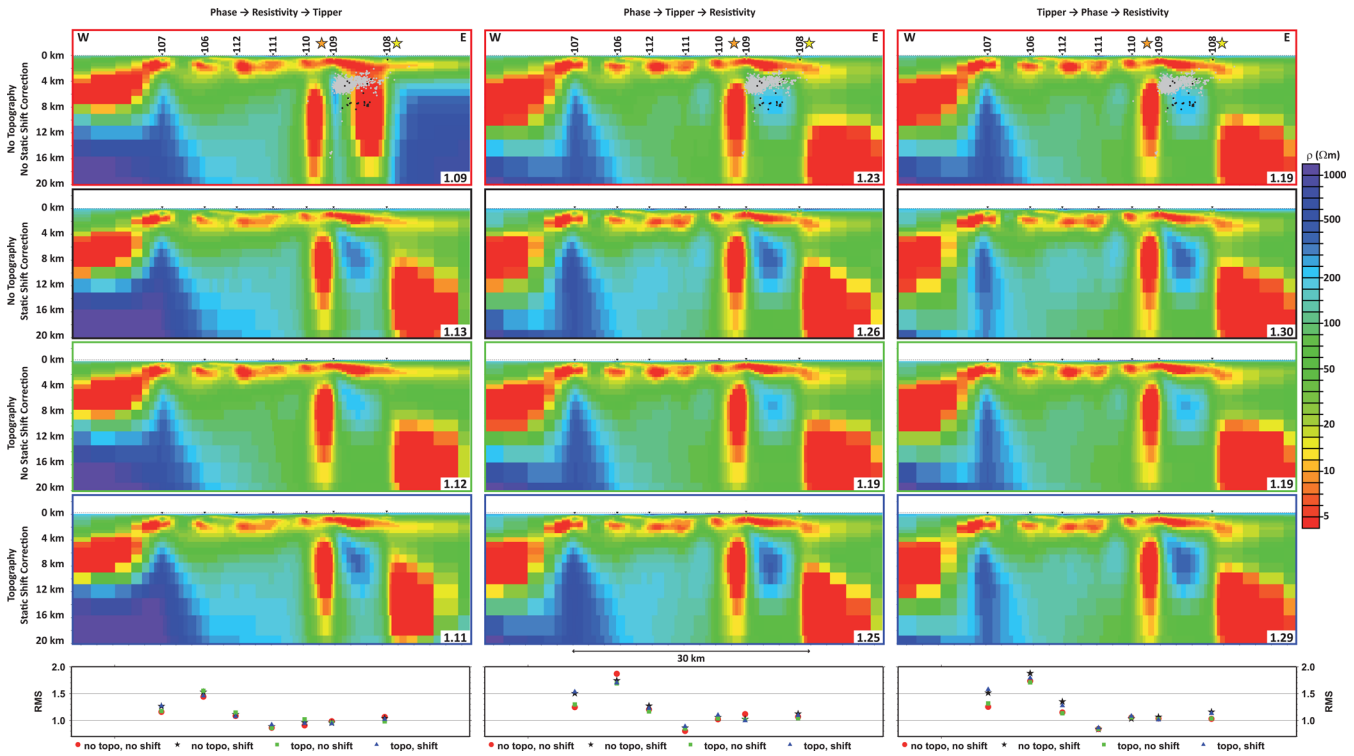

Figure 7. RIVER 2-D inversion models. The inversions are based on the four possible combinations (top to bottom) of meshes with and without topography and shifted and unshifted MT data introduced in different orders [left: order (i), centre: order (ii), right: order (iii) – see text for explanation]. The final rms values are given at the bottom right-hand corner of each model and the individual rms values of each site is plotted below each data introduction sequence (symbol colours correspond to the frame of each model). The yellow and orange stars mark the locations (projected onto the profile) of the flank and summit eruptions, respectively. The black (≤2 km distance to profile) and grey (2–5 km distance to profile) dots are the projected earthquake locations by Tarasewicz *et al.* (2012a,b).

the eastern end of the profile. These structures are considered as implausible. Firstly, all other models agree on a different electrical structure. Secondly, looking at the intermediate inversion models it is obvious that this odd structure is introduced at the stage where ρ_{TE} is added, and as mentioned above, especially TE mode data can cause artefacts in 2-D models if 3-D structures are present. The eastern end of the profile is located at the end of a narrow valley and in between Eyjafjallajökull and Katla as well as in close proximity to the flank eruption site. Therefore, at least at long periods an influence of 3-D structures is possible. Thirdly, this odd structure is mainly related to site 108, which has a strong static shift on the YX component (*cf.* Figs 3 and 5) and the distance to the next site (109) is rather large. Due to the static shift the TM mode data are smaller than the TE mode data for the entire period range. For 2-D models this implies that a resistivity contrast is nearby and the site is located on the more conductive side. Hence, a conductor is introduced and the needed counterpart (i.e. the resistor) can only be placed east of site 108, where no data constrain the resistivity structure. Subsequent introduction of tipper data does not appear to be able to remove these dominant structures. This is a general problem with NLCG methods, once a large structure is in the model it becomes very difficult to remove it; hence structure in the data is introduced 'slowly' in order that structure in the model develops slowly and not rapidly with iteration. If static shift correction and/or topography are applied, the offset between TE and TM mode data is compensated and therefore, a strong resistivity contrast is no longer required to fit the data. For the other two results without topography and correction, ρ_{TE} is the last data subset introduced to the inversion and apparently, the model is already well constrained by the ρ_{TM} and tipper data so that ρ_{TE} cannot enforce a strong change in the structure. Comparing the data fit of the models without and with topography (no shift correction, order i), the data fit at site 108 is very similar but slightly better for the model with topography. The negligible lower rms value for the model without topography is related to minor variations in the resistivity structure beneath sites 106, 110 and 112, and is therefore not related to the questionable structure at the eastern end of the profile.

Beneath the projected location of the summit eruption (orange star on Fig. 7) is a conduit-like, conductive structure present in all models. (Note, the lava flow of the summit eruption came down on the northern flank in between sites 109 and 110.) A discontinuous, near-surface conductive structure is found in all models beneath all sites. Manually connecting this conductor from end-to-end and running a forward calculation shows that the site spacing is too large to judge if the conductor is continuous or discontinuous. A third conductor at about 10 km depth is present to the east of site 108. Although its geometry is not well resolved as it is beyond the end of the profile, forward modelling tests (removing the conductor) showed that such a conductive structure is required to fit the long period data of the eastern sites of the profile. Similar considerations apply to the deeper conductor west of site 107.

Like profile RIVER, the models of profile FIMM are very similar for all 12 options. Accordingly, Fig. 8 only shows one representative model [i.e. mesh with topography, unshifted MT data introduced in order (iii)]. This model also shows the near-surface conductive layer and an increased conductivity at the northern half of the profile. At the centre of the profile the top of the conductor is at about 12 km depth, and towards the north it becomes shallower and more

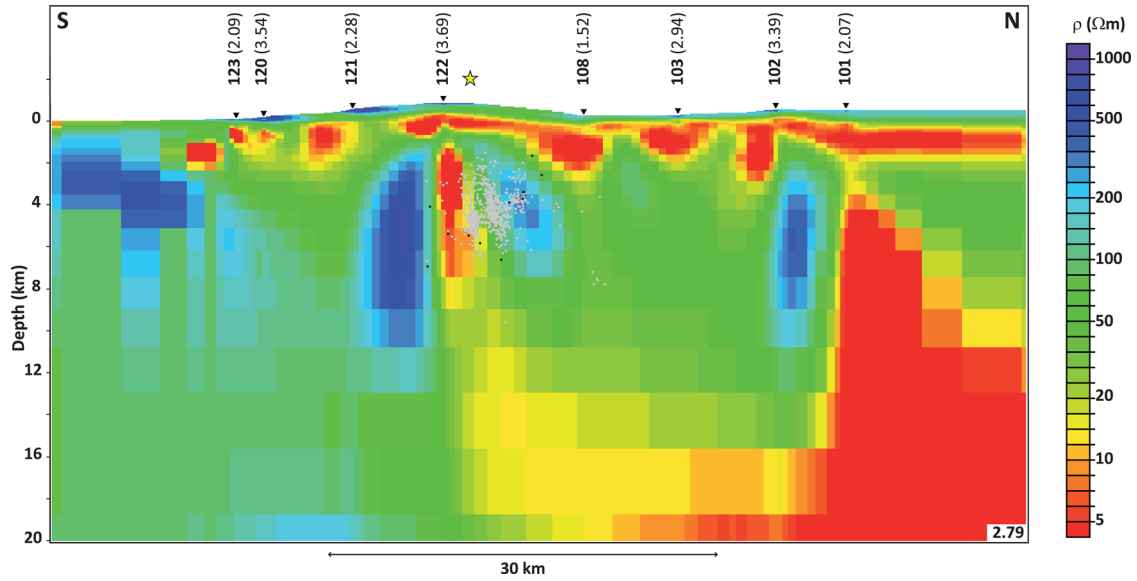

Figure 8. FIMM 2-D inversion model. The inversion is based on a mesh with topography and unshifted MT data introduced in order (iii) (see text for explanation). The final rms value is given at the bottom right-hand corner and the individual rms values of each site are specified in parentheses above the site numbers. The yellow star marks the location (projected onto the profile) of the flank eruption. The black (≤2 km distance to profile) and grey (2–5 km distance to profile) dots are the projected earthquake locations by Tarasewicz *et al.* (2012a,b).

conductive. There is the suggestion of an electrical connection to the near-surface conductor beneath site 101. Forward modelling tests again showed that the conductor is a required structure to explain the data. Beneath site 122 and the flank eruption (yellow star on Fig. 8) a vertical conductor is present that is connected to the deeper conductor. The projected earthquake locations (after Tarasewicz *et al.* 2012a,b) associated with the magma rise of the dyke placement and flank eruption collocate with the edge of this conductor.

For profile COAST, either site 115 or 116 can be used for inversion. Whereas the data for site 115 allows for all 12 options, site 116 only provides unshifted MT data due to lacking TEM data. Fig. 9 shows three representative models [i.e. MT data introduced in order (iii)]. For site 115 models with shifted data and no topography (top) and the opposite, that is unshifted data and topography (middle) are shown. A model of the latter combination, but with site 116, is plotted below. The individual rms values of each site are plotted at the bottom, while the overall rms of each model is stated at the bottom right-hand corner. Comparing both models with topography and unshifted data but sites 115 and 116, respectively, the obtained structures and rms values are—not surprisingly—very similar. The model including the static shifted data from site 115 appears smoother than the others and results in lower rms values; the major improvement in rms error is at sites 117, 118, 120 and 123. Fig. 5 showed strong shifts for sites 117 and 123, which obviously could not be compensated for by the 2-D topography applied in the other models. Furthermore, especially those four sites are located at places where there is strong topography perpendicular to the profile, and hence could not be taken into account for the inversion mesh, but is indirectly considered in the static shift correction. It also cannot be excluded that other causes for static shift than topography are affecting the data at those sites. Nevertheless, the major structures are similar in all models. As seen for the other two profiles there is a near-surface conductive layer; again it is uncertain whether it is laterally continuous or not. West of site 107 a deeper, conductive structure is revealed (analogous to RIVER), but it is beyond the end of the profile and therefore not well resolved. A few (nearly) vertical conductive structures are present in all models but cannot be associated with the flank or summit eruptions. They may be indications of the connection of shallow magma pockets to deeper seated magma reservoirs, as suggested by Spichak *et al.* (2013). The geometries and actual resistivity of the lower crustal resistor between sites 115/116 and 117 is poorly resolved due to the large site spacing. Forward modelling without the resistor only has influence on the long period data, which at least indicates its presence.

6 DISCUSSION

Compared to the studies at Mount St. Helens (Hill *et al.* 2009) and at Mount Ruapehu (Ingham *et al.* 2009) site coverage at Eyjafjallajökull is not ideal. While Hill *et al.* (2009) and Ingham *et al.* (2009) have a rather array-like site distribution, not only around but also on top of the volcanoes and within the crater, the inaccessibility of many areas at Eyjafjallajökull restricted the installation of sites in a regular grid. Nevertheless, the findings at Eyjafjallajökull are similar to those at Mount St Helens and Mount Ruapehu. At all three volcanoes the 2-D MT resistivity models reveal vertical, conductive structures beneath the crater. In all three cases this structure has a width of a few kilometres and a resistivity of a few Ωm, hence most likely underestimating the conductivity of the structure and at the same time overestimation its width (*cf.* comparison of 2-D versus 3-D models by Ingham *et al.* 2009). In all three cases seismic activity is accompanying magma activity. Hill *et al.* (2009) and Ingham *et al.* (2009) interpret the vertical conductive zones as narrow volcanic conduits supplying Mount St Helens and Mount Ruapehu, respectively.

A few years after eruption, measurements at Usu-Shinzan volcano on Hokkaido, Japan by Watanabe *et al.* (1984) revealed a conductor that they interpreted as magma intrusion associated with this event, while several years later this area appeared as resistive, likely due to cooling of the magma (Matsushima *et al.* 2001). Therefore, although the measurements at Eyjafjallajökull took place

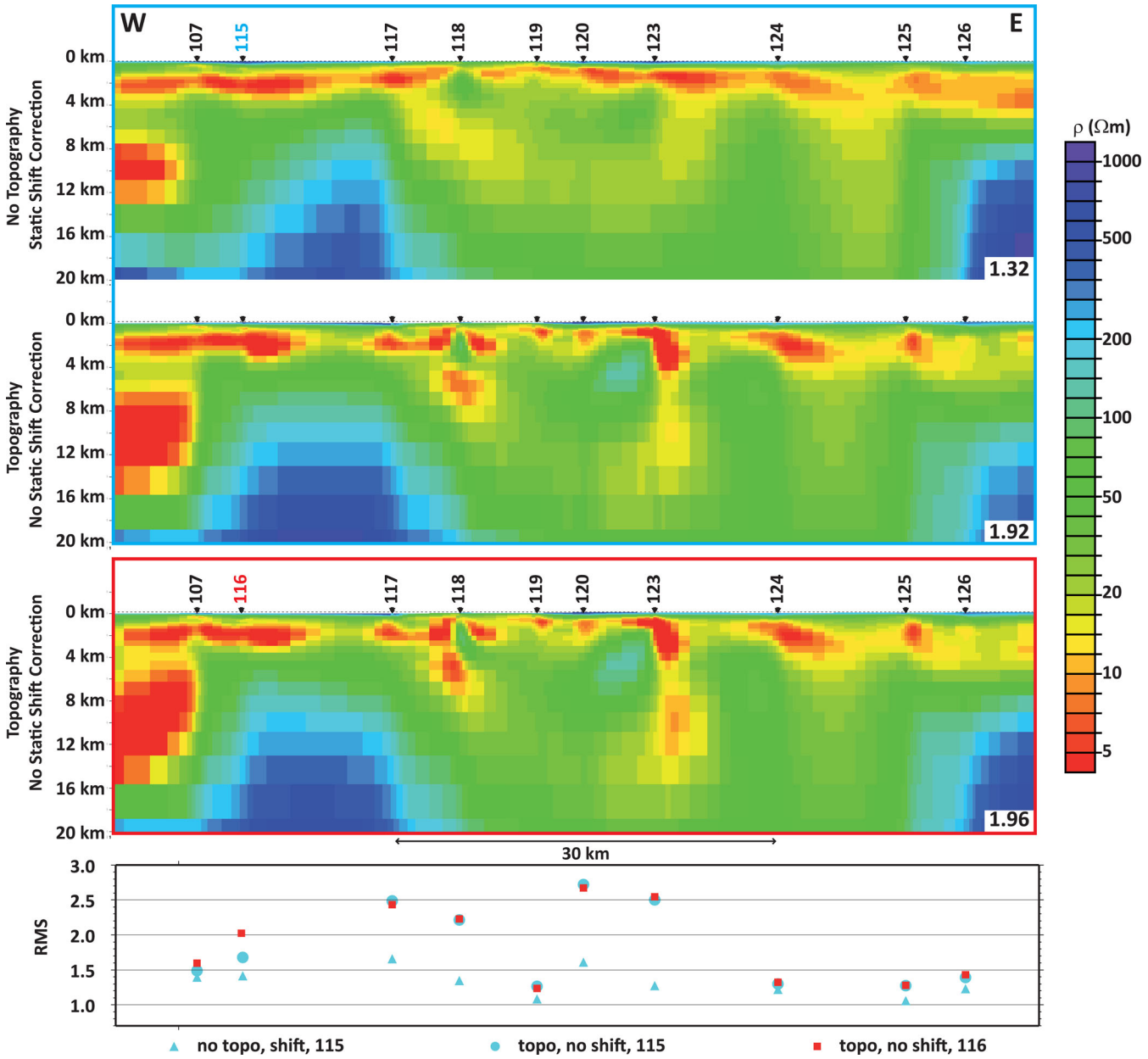

Figure 9. COAST 2-D inversion models. Site 115 (blue) in top two models is replaced by site 116 in the model below (red). For all three models the MT data are introduced in order (iii) (see text for explanation). While the top model is based on shifted MT data and a mesh without topography, both other models used topography but unshifted data. The final rms values of each model are given at the bottom right-hand corner and the individual rms values of each site are shown at the bottom.

about 1 yr after eruption, the conductive structures still can be associate with the magma intrusions of the 2010 events. Nevertheless, any assumptions about the width of the conduit and its resistivity (and maybe even the melt fracture) are rather notional. First of all the conduit is a structure a few kilometres aside the profile, and secondly, it is a 3-D structure while all possible estimates can only be based on 2-D resistivity models and 2-D assumptions. Based on laboratory studies by, for example, Schilling *et al.* (1997) and ten Grotenhuis *et al.* (2005) the resistivities of melt can be estimated as follows: Pure melt has a resistivity of ∼0.1 Ωm (high conducting melt) to ∼0.2 Ωm (low conducting melt). At melt fractions above a few per cent by volume the resistivity of the partially molten rock is nearly independent of the conductivity of the solid phase. The resistivity for ≥10 per cent melt can be approximated by 1 Ωm. The conductive structure in the 2-D models is approximately 2 km wide; horizontally averaging the resistivity over this width at different depths and for several models suggests a resistivity in the range 0.56–11 Ωm. Clearly the resistivity and/or width of this structure is not constant but varies with depth. Also note that resolution of the 2-D models is limited by mesh discretization (e.g. those 2 km width are discretized by six cells). Fig. 10 shows resistivity-width relations based on 2-D average resistivities of 0.56, 5 and 11 Ωm and illustrates the following discussion. Based on the extreme case with pure melt and an average resistivity of 11 Ωm (blue line) for the 2 km structure, it is clear that the structure must be at least ∼20 m wide (i.e. a resistivity of 0.1 Ωm distributed over 20 m). Its width increases with a more realistic assumption regarding the melt fraction and also with decreasing average resistivity of the 2-D structure.

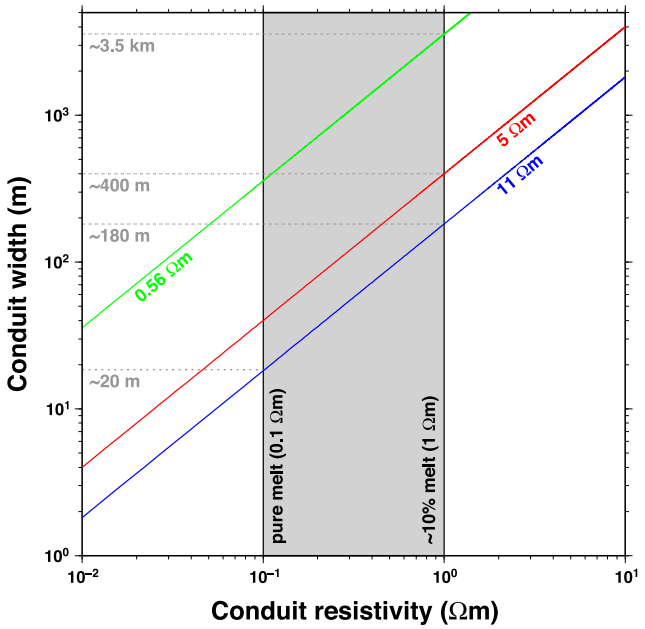

Figure 10. Conduit width versus conduit resistivity. This plot illustrates the speculative estimates of the conduit width described in the text. The resistivity range from pure melt to 10 per cent melt (based on Schilling *et al.* 1997; ten Grotenhuis *et al.* 2005) is shown as grey shaded area. (Note, the relationship between the decreasing resistivity and the increasing melt fraction is not linear.) The coloured lines represent the estimated resistivity-width relations based on the maximum (blue, 11 Ωm), minimum (green, 0.56 Ωm) and intermediate (red, 5 Ωm) average resistivities extracted from the 2-D models. The widths mentioned in the text are labelled in grey.

Assuming ≥10 per cent melt fraction (i.e. 1 Ωm) the width ranges from ∼180 m (average resistivity 11 Ωm; blue line) to ∼3.5 km (average resistivity 0.56 Ωm; green line). For an intermediate average resistivity of 5 Ωm (red line) and ≥10 per cent melt fraction the resulting width would be about 400 m.

None of the models of all three profiles, neither 1-D nor 2-D, is able to resolve a conductive structure in the depth range of about 4–5.9 km that could be interpreted as the sill layers suggested by Sigmundsson *et al.* (2010). Thus if present the sill layers are either too thin or the resistivity contrast to the surrounding background is not great enough or both. Considering the volume increase and the outlined horizontal extension of the sills by Sigmundsson *et al.* (2010), the thickness of the sills is only in the decimetre range. This is also consistent with thicknesses found by Pedersen & Sigmundsson (2004) for older sills at Eyjafjallajökull. Forward modelling introducing a 1 Ωm layer in about 5 km depth showed that only for a minimum thickness of 10–15 m minor discrepancies in response become visible. Hence, the sill layers are most likely too thin to be resolved.

To distinguish whether the near-surface conductive structures are a continuous layer or disconnected a denser site spacing is required. The conductors at about 10 km depth (profiles RIVER and FIMM) may be partly molten basalts that are trapped in ductile intrusive rocks (Árnason *et al.* 2010; Spichak *et al.* 2013). The near-surface conductive layer (profiles RIVER, FIMM and COAST) could, according to Spichak *et al.* (2013), represent the shallow magma pockets at 1–2 km depth that are connected by vertical or near-vertical conduits with the lower layer. Such connections between the two conductors can be found in profiles RIVER and FIMM (and also indicated in COAST). But more likely the shallow conductors reflect low temperature (100–240 °C) hydrothermal alteration minerals (e.g. smectite and zeolite that have high CEC—that is cation-exchange capacity) due to the cooling of magmatic intrusions. The resistivity increase beneath this layer is related to the change in alteration type—namely high temperature (above 240 °C) hydrothermal alteration minerals (e.g. chlorite and epidote that have low CEC; Árnason *et al.* 2010). Also, according to a seismic refraction survey by Flóvenz (1981) at the south coast of Iceland, Eyjafjallajökull and Katla are at least partly built on conductive marine sediments that are present down to 1.5–2.7 km depth. Therefore, the enhance conductivity observed at shallow depths can also be (at least partly) related to the marine sediments.

Comparison with earthquake locations showed good agreement for the dyke location. Whereas earthquakes indicate locations of stress release (i.e. most likely at the interface of dyke and surrounding rocks), EM methods image the conductivity anomalies caused by the magmatic volume, either directly or indirectly (release of fluids). Furthermore, seismicity is present only during magma movement (i.e. mainly prior and during the eruption) and therefore, instrumentation, has to be in place before an eruption occurs. This study has demonstrated that EM methods—even 1 yr after the event—allow identification of conduit and dyke structures. In general, EM methods thus offer great potential for investigation of volcanic eruptions, even if only few data were acquired prior to and during the eruption. Repeat measurements or continuous monitoring will likely be able to detect changes in resistivity structure related to magma recharge and settling of the volcanic system (e.g. Jackson *et al.* 1985; Utada *et al.* 2007).

Although magma compositions, seismic velocities and the complex formation history suggest a heterogeneous subsurface, the derived resistivity models do not present a strong resistivity contrast distribution, and all the MT tools we have applied suggested rather 1-D subsurface conditions for the first three decades of data. It thus appears that the resistivity structures are likely dominated by hydrothermal alteration and temperature effects rather than by the heterogeneity of the rocks. Furthermore, the heterogeneity might be too small in scale (similar to the sill thickness) to be resolved, instead an averaged image is produced from the integrating nature of EM. No critical information important to the debate regarding thin versus thick crust was found.

For a more detailed image of the resistivity structure a denser site distribution is required. To allow an interpretation regarding Katla volcano more sites are required around it but additionally, and importantly, directly on the glacier Mýrdalsjökull. For 3-D modelling, a more equally spaced array with shorter distances between sites is needed but it is logistically impractical (i.e. many areas are hardly accessible, and some not at all, and steep slopes hinder the system installation).

7 CONCLUSIONS

This EM study images for the first time the resistivity structure of the Eyjafjallajökull volcanic system. Although data were recorded about 1 yr after the 2010 eruptions, vertical conductive structures are still present in all derived models indicating the dyke and the conduit of the flank and summit eruptions, respectively. A near-surface conductive layer (at 1–2 km depth), and in some parts a lower second conductor (at about 10–12 km depth), are found. A connection between the two is indicated in the resistivity models, but is weakly

resolved and is not a robust feature. Although a closer site spacing and better spatial coverage of the entire Eyjafjallajökull–Katla system is desirable for more detailed interpretation, this study clearly shows the value of EM investigation to enhance the understanding of such a volcanic system.

ACKNOWLEDGEMENTS

We would like to thank Mark R. Muller, Halldór Örvar Stefánsson, Pálmar Sigurðsson, Sigurbjörn Bogi Jónsson, Alae-Eddine Barkaoui, Anna Wairimu Mwangi, Diego A. Badilla Elizondo, Raymond M. Mwakirani for their time and effort during the fieldwork. We are grateful that Jon Tarasewicz made his earthquake locations available to us. And last but not least we thank Magnús T. Gumundsson and Malcolm Ingham for their constructive reviews of the manuscript.

REFERENCES

Allen, R.M. *et al.*, 2002. Plume-driven plumbing and crustal formation in Iceland, *J. geophys. Res.,* **107**(B8), doi:10.1029/2001JB000584.

Árnadóttir, T. *et al.*, 2008. Capturing crustal deformation signals with a new high-rate continuous GPS network Iceland, *EOS, Trans. Am. geophys. Un.,* **89**(53), Fall Meet. Suppl., Abstract G43A–0650.

Árnason, K., Eysteinsson, H. & Hersir, G.P., 2010. Joint 1D inversion of TEM and MT data and 3D inversion of MT data in the Hengill area, SW Iceland, *Geothermics,* **39,** 13–34.

Baba, K., Chave, A.D., Evans, R.L., Hirth, G. & Mackie, R.L., 2006. Mantle dynamics beneath the East Pacific Rise at 17°S: insights from the Mantle Electromagnetic and Tomography (MELT) experiment, *J. geophys. Res.,* **111,** B02101, doi:10.1029/2004JB003598.

Bailey, R.C. & Groom, R.W., 1987. Decomposition of the magnetotelluric impedance tensor which is useful in the presence of channelling, in *Proceedings of the 57th Annual International Society of Exploration Geophysicists Meeting and Exposition,* Expanded Abstracts, Vol. 57, pp. 154–156, Tulsa, OK.

Båth, M., 1960. Crustal structure of Iceland, *J. geophys. Res.,* **65,** 1793–1807.

Beblo, M. & Björnsson, A., 1978. Magnetotelluric investigation of the lower crust and upper mantle beneath Iceland, *J. Geophys.,* **45,** 1–16.

Beblo, M. & Björnsson, A., 1980. A model of electrical resistivity beneath NE Iceland, correlation with temperature, *J. Geophys.,* **47,** 184–190.

Berdichevsky, M.N. & Dmitriev, V.I., 1976a. Basic principles of interpretation of magnetotelluric sounding curves, in *Geoelectric and Geothermal Studies,* pp. 165–221, ed. Adam, A., KAPG Geophysical Monograph, Akadémiai Kiadó.

Berdichevsky, M.N. & Dmitriev, V.I., 1976b. Distortion of magnetic and electrical fields by near-surface lateral inhomogeneities, *Acta Geod., Geophys. Montan., Acad. Sci. Hungary,* **11,** 447–483.

Berdichevsky, M.N., Bezruk, I.A. & Chinavera, O.M., 1973. Magnetotelluric sounding with the use of mathematical filters, *Izv. Akad. Nauk. SSSR Fiz. Zeml.,* **3,** 72–92 (in Russian).

Bertrand, E., Caldwell, T.G., Hill, G.J. & Bennie, S.L., 2013. 3-d inversion of a 200+ site magnetotelluric array for deep geothermal exploration, in *Proceedings of the 5th International Symposium on Three-Dimensional Electromagnetics,* Sapporo, Japan.

Bjarnason, I.T., Menke, W., Flóvenz, Ó.G. & Caress, D., 1993. Tomographic image of the mid-Atlantic plate boundary in southwestern Iceland, *J. geophys. Res.,* **98,** 6607–6622.

Björnsson, A., Eysteinsson, H. & Beblo, M., 2005. Crustal formation and magma genesis beneath Iceland: magnetotelluric constraints, in *Plates, Plumes, and Paradigms,* Vol. 388 of Geophysical Society of America Special Paper.

Björnsson, H., Pálsson, F. & Gudmundsson, M.T., 2000. Surface and bedrock topography of the Mýrdalsjökull ice cap, Iceland: the Katla caldera, eruption sites and routes of Jökulhlaups, *Jökull,* **49,** 29–46.

Brandsdóttir, B., Menke, W., Einarsson, P., White, R. & Staples, R.K., 1997. Færoe-Iceland ridge experiment, 2. Crustal structure of the Krafla central volcano, *J. geophys. Res.,* **102,** 7867–7886.

Caldwell, T.G., Bibby, H.M. & Brown, C., 2004. The magnetotelluric phase tensor, *Geophys. J. Int.,* **158,** 457–469.

Chave, A.D. & Jones, A.G., 1997. Electric and magnetic field galvanic distortion decomposition of BC87 data, *J. Geomagn. Geoelectr.,* **49,** 767–789.

Chave, A.D. & Jones, A.G. eds, 2012. *The Magnetotelluric Method: Theory and Practice,* Cambridge Univ. Press.

Constable, S.C., Parker, R.L. & Constable, C.G., 1987. Occam's inversion: a practical algorithm for generating smooth models from electromagnetic sounding data, *Geophysics,* **52**(3), 289–300.

Cook, R.D., 1977. Detection of influential observation in linear-regression, *Technometrics,* **19,** 15–18.

Dahm, T. & Brandsdóttir, B., 1987. Moment tensors of micro-earthquakes from the Eyjafjallajökull volcano in South Iceland, *Geophys. J. Int.,* **130**(1), 183–192.

Darbyshire, F.A., Bjarnason, I.T., White, R.S. & Flóvenz, Ó.G., 1998. Crustal structure above the Iceland mantle plume imaged by the ICEMELT refraction profile, *Geophys. J. Int.,* **135,** 1131–1149.

Darbyshire, F.A., Priestley, K.F., White, R.S., Stefansson, R., Gudmundsson, G.B. & Jakobsdóttir, S.S., 2000a. Crustal structure of central and northern Iceland from analysis of teleseismic receiver functions, *Geophys. J. Int.,* **143,** 163–184.

Darbyshire, F.A., White, R.S. & Priestley, K.F., 2000b. Structure of the crust and uppermost mantle of Iceland from a combined seismic and gravity study, *Earth planet. Sci. Lett.,* **181,** 409–428.

Davis, J.W., Jones, A.G., Bleeker, W. & Grütter, H., 2003. Lithosphere development in the Slave craton: a linked crustal and mantle perspective, *Lithos,* **71**(2–4), 575–589.

de Lugão, P.P. & Kriegshäuser, B., 1997. 2-D inversion of magnetotelluric data over 3-D structures, in *Proceedings of the 67th Ann. Internat. Mtg. Soc. of Expl. Geophys.,* Expanded Abstract, pp. 382–385.

DeMets, C., Gordon, R.G., Argus, D.F. & Stein, S., 1994. Effect of recent revisions to the geomagnetic reversal time scale on estimates of current plate motion, *Geophys. Res. Lett.,* **21**(20), 2191–2194.

Duojun, W., Heping, L., Li, Y., Weigang, Z., Congqiang, L., Gengli, S. & Dongye, D., 2002. The electrical conductivity of gabbro at high temperature and high pressure, *Chin. J. Geochem.,* **21**(3), 5–12.

Edwards, B., Magnússon, E., Thordarson, T., Gumundsson, M.T., Höskuldsson, A., Oddsson, B. & Haklar, J., 2012. Interaction between lava and snow/ice during the 2010 Fimmvörðuháls eruption, south-central Iceland, *J. geophys. Res.,* **117,** B04302, doi:10.1029/2011JB008985.

Einarsson, P. & Brandsdóttir, B., 2000. Earthquakes in the Mýrdalsjökull area, Iceland, 1978–1985: seasonal correlation and relation to volcanoes, *Jökull,* **49,** 59–73

Elíasson, J., Larsen, G., Gumundsson, M.T. & Sigmundsson, F., 2006. Probablistic model for eruptions and associated flood events in the Katla caldera, Iceland, *Comput. Geosci.,* **10,** 179–200.

Evans, R.L., Hirth, G., Baba, K., Forsyth, D., Chave, A. & Mackie, R., 2005. Geophysical evidence from the MELT area for compositional controls on oceanic plates, *Nature,* **437,** 249–252.

Eysteinsson, H. & Hermance, J.F., 1985. Magnetotelluric measurements across the eastern neovolcanic zone in southern Iceland, *J. geophys. Res.: Solid Earth,* **90,** 10 093–10 103.

Fedorova, T., Jacoby, W.R. & Wallner, H., 2005. Crust-mantle transition and Moho model for Iceland and surroundings from seismic, topography, and gravity data, *Tectonophysics,* **396,** 119–140.

Ferguson, I.J., Jones, A.G. & Chave, A.D., 2012. Case histories and geological applications, in *The Magnetotelluric Method: Theory and Practice,* Chap. 10, pp. 480–544, eds Chave, A.D. & Jones, A.G., Cambridge Univ. Press.

Flóvenz, Ó.G., 1980. Seismic structure of the icelandic crust above layer three and the relation between body wave velocity and the alteration of basaltic crust, *J. Geophys.,* **47,** 211–220.

Flóvenz, Ó.G., 1981. Setög undir suðurströnd Íslands, *Náttúrufraedingurinn,* **51,** 169–177.

Flóvenz, Ó.G. & Gunnarsson, K., 1991. Seismic crustal structure in Iceland and the surrounding area, *Tectonophysics,* **189,** 1–17.

Flóvenz, Ó.G. & Sæmundsson, K., 1993. Heat flow and geothermal processes in Iceland, *Tectonophysics,* **225,** 123–138.

Galeczka, I., Oelkers, E.H. & Gislason, S.R., 2014. The chemisrty and element fluxes of the July 2011 Múlakvísl and Kaldakvísl glacial floods, Iceland, *J. Volc. Geotherm. Res.,* **273,** 41–57.

Garcia, X. & Jones, A.G., 2002. Decomposition of three-dimensional magnetotelluric data, in *Three-Dimensional Electromagnetics,* Vol. 35 of Methods in Geochemistry and Geophysics, Chap. 13, pp. 235–250, eds Zhdanov, M.S. & Wannamaker, P.E., Elsevier.

Garcia, X., Ledo, J. & Queralt, P., 1999. 2D inversion of 3D magnetotelluric data: the Kayabe dataset, *Earth, Planets Space,* **51,** 1135–1143.

Gebrande, H., Miller, H. & Einarsson, P., 1980. Seismic structure of Iceland along RRISP-Profile 1, *J. Geophys.,* **47,** 239–249.

Groom, R.W., 1988. The effects of inhomogeneities on magnetotellurics, *PhD thesis,* University Toronto, Canada.

Groom, R.W. & Bailey, R.C., 1989. Decomposition of Magnetotelluric Impedance Tensors in the Presence of Local Three-Dimensional Galvanic Distortion, *J. geophys. Res.: Solid Earth,* **94**(B2), 1913–1925.

Gudmundsson, M.T., Elíasson, J., Larsen, G., Gylfason, A.G., Einarsson, P., Jóhannesson, T., Hákonardóttir, K.M. & Jóhannesson, H., 2005. Yfirlit um hættu vegna eldgosa og hlaupa frá vesturhluta Mýrdalsjökls og Eyjafjallajökli, in *Hættumat vegna eldgosa og hlaupa frá vestanverdum Mýrdalsjökli og Eyjafjallajökli,* Icelandic Collection, Chap. 1, pp. 11–44, eds Gudmundsson, M.T. & Gylfason, A.G., Fiske (in Icelandic).

Gudmundsson, M.T., Hógnadóttir, P., Kristinsson, A.B. & Gudbjórnsson, S., 2007. Geothermal activity in the subglacial Katla caldera, Iceland, 1999–2005, studied with radar altimetry, *Ann Glaciol.,* **45,** 66–72.

Gudmundsson, M.T. *et al.*, 2012a. Scientific aspects: Discussion and analysis, in *The 2010 Eyjafjallajökull eruption, Iceland,* Chap. 5.1, pp. 101–114, ed. orkelsson, B., Iceland Meterological Office, Institute of Earth Science University of Iceland, Department of Civil Protection of National Commissioner of the Icelandic Police, Available at: http://en.vedur.is/media/ICAOreport_web_lr.pdf.

Gudmundsson, M.T. *et al.*, 2012b. Ash generation and distribution from April - May 2010 eruption of Eyjafjallajökull, Iceland, *Scient. Rep.,* **2,** doi:10.1038/srep00572.

Gudmundsson, O., Brandsdóttir, B., Menke, W. & Sigvaldason, G.E., 1994. The crustal magma chamber of the Katla volcano in South Iceland revealed by 2-D seismic undershooting, *Geophys. J. Int.,* **119,** 277–296.

Hamilton, M.P. *et al.*, 2006. Electrical anisotropy of South African lithosphere compared with seismic anisotropy from shear-wave splitting analyses, *Phys. Earth planet. Inter.,* **158,** 226–239.

Hermance, J.F., 1982. The asymptotic response of 3-dimensional basin offsets to magnetotelluric fields at long periods—the effects of current channeling, *Geophysics,* **47,** 1562–1573.

Hermance, J.F. & Grillot, L.R., 1974. Constraints of temperatures beneath Iceland from magnetotelluric data, *Phys. Earth planet. Inter.,* **8,** 1–12.

Hersir, G.P., Björnsson, A. & Pedersen, L.B., 1984. Magnetotelluric survey across the active spreading zone in southwestern Iceland, *J. Volc. Geotherm. Res.,* **20,** 253–265.

Hersir, G.P., Árnason, K. & Vilhjálmsson, A.M., 2013. 3D inversion of magnetotelluric (MT) resistivity data from Krýsuvík high temperature geothermal area in SW Iceland, in *Proceedings of the 38th Workshop on Geothermal Reservoir Enineering,* Stanford Univ., Stanford, 14 pp.

Hill, G.J., Caldwell, T.G., Heise, W., Chertkoff, D.G., Bibby, H.M., Burgess, M.K., Cull, J.P. & Cas, A.F., 2009. Distribution of melt beneath Mount St. Helens and Mount Adams inferred from magnetotelluric data, *Nat. Geosci.,* **2,** 785–789.

Hjaltadóttir, S. & Vogfjörd, K.S., 2010. Seismic evidence of magma transport in Eyjafjallajökull during 2009–2010, in *Abstract V21F-02 presented at 2010 Fall Meeting,* AGU, San Francisco, CA, 13–17 December.

Hjaltadóttir, S., Hreinsdóttir, S., Brandsdóttir, B., Ófeigsson, B.G., Pedersen, R., Eiríksdóttir, E.S. & Gudmundsson, M.T., 2012. 2010 pre-eruption phase, in *The 2010 Eyjafjallajökull Eruption, Iceland,* Chap. 4.2, pp. 49–54, ed. orkelsson, B., Iceland Meterological Office, Institute of Earth Science University of Iceland, Department of Civil Protection of National Commissioner of the Icelandic Police, Available at: http://en.vedur.is/media/ICAOreport_web_lr.pdf.

Hooper, A., 2008. A multi-temporal InSAR method incorporating both persistent scatterer and small baseline approaches, *Geophys. Res. Lett.,* **35,** L16302, doi:10.1029/2008GL034654.

Hooper, A., Pedersen, R. & Sigmundsson, F., 2009. Constraints on magma intrusion at Eyjafjallajökull and Katla volcanoes in Iceland, from time series SAR interferometry, in *VOLUME project, EU PF6 (No. 018471),* eds Bean, C.J., Braiden, A.K., Lokmer, I., Martini, F. & O'Brien, G.S., VOLUME Project Consortium, Dublin.

Ingham, M.R., Bibby, H.M., Heise, W., Jones, K.A., Cairns, P., Dravitzki, S.S.L., Bennie, T.G.C. & Ogawa, Y., 2009. A magnetotelluric study of Mount Ruapehu volcano, New Zealand, *Geophys. J. Int.,* **179,** 887–904.

Jackson, D.B., Kauahikaua, J. & Zablocki, C.J., 1985. Resistivity monitoring of an active volcano using the controlled-source electromagnetic technique: Kilauea Hawaii, *J. geophys.. Res.: Solid Earth,* **90,** 12 545–12 555.

Jiracek, G.R., 1990. Near-surface and topographic distortions in electromagnetic induction, *Surv. Geophys.,* **11,** 163–203.

Jödicke, H., 1992. Water and graphite in the Earth's crust—an approach to interpretation of conductivity models, *Surv. Geophys.,* **13,** 381–407.

Jóhannesson, H., 1980. Evolution of rift zones in western Iceland, *Náttúrufrdingurinn,* **50,** 13–31.

Jóhannesson, H. & Saemundsson, K., 1999. *Geological map 1:100.000*, Icelandic Institute of Natural History.

Jones, A.G., 1988. Static shift of magnetotelluric data and its removal in a sedimentary basin environment, *Geophysics,* **53,** 967–978.

Jones, A.G., 2012. Distortion of magnetotelluric data: its identification and removal, in *The Magnetotelluric Method: Theory and Practice,* Chap. 6, pp. 219–302, eds Chave, A.D. & Jones, A.G., Cambridge Univ. Press.

Jones, A.G. & Craven, J.A., 1990. The North American Central Plains conductivity anomaly and its correlation with gravity, magnetic, seismic, and heat flow data in Saskatchewan, Canada, *Phys. Earth planet. Inter.,* **60,** 169–194.

Jones, A.G. & Dumas, I., 1993. Electromagnetic images of a volcanic zone, *Phys. Earth planet. Inter.,* **81,** 289–314.

Jones, A.G. & Jödicke, H., 1984. Magnetotelluric transfer function estimation improvement by a coherence-based rejection technique, in *Proceedings of the 54th Ann. Mtg. Soc. of Expl. Geophys.,* Atlanta, Georgia.

Jones, A.G., Chave, A.D., Egbert, G., Auld, D. & Bahr, K., 1989. A Comparison of techniques for magnetotelluric response function estimation, *J. geophys. Res.: Solid Earth,* **94**(10), 14 201–14 213.

Jónsson, G. & Kristjánsson, L., 2000. Aeromagnetic measurements over Mýrdalsjökull and vicinity, *Jökull,* **49,** 47–58.

Kaban, M.K., Flóvenz, O.G. & Pálmason, G., 2002. Nature of the crust-mantle transition zone and the thermal state of the upper mantle beneath Iceland from gravity modelling, *Geophys. J. Int.,* **149,** 281–299.

Keiding, J.K. & Sigmarsson, O., 2012. Geothermobarometry of the 2010 Eyjafjallajökull eruption, *J. geophys. Res.,* **117,** B00C09, doi:10.1029/2011JB008829.

Kreutzmann, A., Schmeling, H., Junge, A., Ruedas, T., Marquart, G. & Bjarason, I.T., 2004. Temperature and melting of a rigde-centred plume with application to Iceland. Part II: predictions for electromagnetic and seismic observables, *Geophys. J. Int.,* **159,** 1097–1111.

Larsen, G., 2000. Holocene eruptions within the Katla volcanic system, south Iceland: characteristics and environmental impact, *Jökull,* **49,** 1–28.

Larsen, G., Dugmore, A. & Newton, A., 1999. (geochemistry of historical-age silicoc tephras in Iceland, *Holocene,* **9**(4), 463–471.

Larsen, G., Pedersen, R. & Ilyinskaya, E., 2012. The Eyjafjallajökull volcano, in *The 2010 Eyjafjallajökull eruption, Iceland,* Chap. 4.1, pp. 45–48, ed. orkelsson, B., Iceland Meterological Office, Institute of Earth Science University of Iceland, Department of Civil Protection of National Commissioner of the Icelandic Police, Available at: http://en.vedur.is/media/ICAOreport_web_lr.pdf.

Ledo, J., 2005. 2-D versus 3-D magnetotelluric data interpretation, *Surv. Geophys.,* **26,** 511–543.

Ledo, J., Queralt, P., Marti, A. & Jones, A.G., 2002. Two-dimensional interpretation of three-dimensional magnetotelluric data: an example of limitations and resolution, *Geophys. J. Int.,* **150**(1), 127–139.

Mackie, R.L., 2002. User Manual and Software Documentation for Two-Dimensional Inversion of Magnetotelluric data. Anisotropy Version 6.7, GSY-USA, Inc., 2261 Market St., PMB 643, San Francisco, CA 94114, USA.

Matsushima, N., Oshima, H., Ogawa, Y., Takakura, S., Satoh, H., Utsugi, M. & Nishida, Y., 2001. Magma prospecting in Usu volcano, Hokkaido, Japan, using magnetotelluric soundings, *J. Volc. Geotherm. Res.,* **109,** 263–277.

McNeice, G.W. & Jones, A.G., 2001. Multisite, multifrequency tensor decomposition of magnetotelluric data, *Geophysics,* **66**(1), 158–173.

Menke, W., 1999. Crustal isostasy indicates anomalous densities beneath Iceland, *Geophys. Res. Lett.,* **26**(9), 1215–1218.

Menke, W. & Levin, V., 1994. Cold crust in a hotspot, *Geophys. Res. Lett.,* **21,** 1967–1970.

Menke, W., Levin, V. & Sethi, R., 1995. Seismic attenuation in the crust at the mid-Atlantic plate boundary in south west Iceland, *Geophys. J. Int.,* **126,** 175–182.

Miensopust, M.P., Jones, A.G., Muller, M.R., Garcia, X. & Evans, R.L., 2011. Lithospheric structures and Precambrian terrane boundaries in northeastern Botswana revealed through magnetotelluric profiling as part of the Southern African Magnetotelluric Experiment, *J. geophys. Res.,* **116,** B02401, doi: 10.1029/2010JB007740.

Oskarsson, B.V., Gudmundsson, M.T. & Thordarson, T., 2010. The 10th century Skerin ridge on northwest Eyjafjallajökull, south Iceland—volcanic architecture and bimodal magma composition, American Geophysical Union, Fall Meeting 2010.

Pálmason, G., 1971. *Crustal Structure of Iceland from Exploration Seismology,* Soc. Sci. Isl

Park, S.K. & Mackie, R.J., 1997. Crustal structure at Nanga Parbat, northern Pakistan, from magnetotelluric soundings, *Geophys. Res. Lett.,* **24,** 2415–2418.

Parker, R.L., 1980. The inverse problem of electromagnetic induction: existance and construction of solutions based on incomplete data., *J. geophys. Res.,* **85,** 4421–4425.

Parker, R.L., 1982. The existence of a region inaccessible to magnetotelluric sounding, *Geophys. J. R. astr. Soc.,* **68,** 165–170.

Pavlenkova, N.I. & Zverev, S.M., 1981. Seismic model of Iceland's crust, *Geol. Rundschau,* **70,** 271–281.

Pedersen, R. & Sigmundsson, F., 2004. InSAR based sill model links spatially offset areas of deformation and seismicity for the 1994 unrest episode at Eyjafjallajökull volcano, Iceland, *Geophys. Res. Lett.,* **31,** L14610, doi:10.1029/2004GL020368.

Pedersen, R. & Sigmundsson, F., 2006. Temporal development of the 1999 intrusive episode in the Eyjafjallajökull volcano, Iceland, derived from InSAR images, *Bull. Volcanol.,* **68,** 377–393.

Pellerin, L. & Hohmann, G.W., 1990. Transient electromagnetic inversion: A remedy for magnetotelluric static shifts, *Geophysics,* **55**(9), 1242–1250.

Rodi, W. & Mackie, R.L., 2001. Nonlinear conjugate gradients algorithm for 2-D magnetotelluric inversion, *Geophysics,* **66**(1), 174–187.

Rousseeuw, P.J., 1984. Least median of squares regression, *J. Am. Stat. Assoc.,* **79,** 871–880.

Rousseeuw, P.J. & Leroy, A.M., 1987. *Robust Regression and Outlier Detection,* Wiley.

Schilling, F.R., Partzsch, G.M., Brasse, H. & Schwarz, G., 1997. Partial melting below the magmatic arc in the central Andes deduced from geoelectromagnetic field experiments and laboratory data, *Phys. Earth planet. Inter.,* **103,** 17–31.

Schreiber-Enslin, S.E., LaFemina, P.C., Sturkell, E., Hooper, A.J. & Webb, S.J., 2011. Geodetic investigation of plate spreading along a propagating ridge: the Eastern Volcanic Zone, Iceland, *Geophys. J. Int.,* **187,** 1175–1194.

Schwarz, G., 1990. Electrical conductivity of the earth's crust and upper mantle, *Surv. Geophys.,* **11,** 133–161.

Sella, G.F., Dixon, T.H. & Mao, A., 2002. REVEL: a model for recent plate velocities from space geodesy, *J. geophys. Res.,* **107**(B4), doi:10.1029/2000JB000033.

Selway, K., 2014. On the causes of electrical conductivity anomalies in tectonically stable lithosphere, *Surv. Geophys.,* **35,** 219–257.

Shankland, T.J., 1975. Electrical conduction in rocks and minerals: parameters for interpretation, *Phys. Earth planet. Inter.,* **10,** 209–219.

Sigmarsson, O., Vlastelic, I. & Devidal, J., 2010. Trace-element variations reveal dynamic magma mixing during the 2010 eruption of Eyjafjallajökull, Iceland, *EOS, Trans. Am. geophys. Un.,* **91,** Fall meet. Suppl., abstract V21F-04.

Sigmarsson, O. *et al.*, 2011. Remobilization of silicic intrusion by mafic magmas during the 2010 Eyjafjallajökull eruption, *J. geophys. Res.: Solid Earth,* **2,** 271–281.

Sigmundsson, F. *et al.*, 2010. Intrusion triggering of the 2010 Eyjafjallajökull explosive eruption, *Nature,* **468,** 426–432.

Smith, J.T., 1997. Estimating galvanic-distortion magnetic fields in magnetotellurics, *Geophys. J. Int.,* **130,** 65–72.

Spichak, V.V., Zakharov, O.K. & Goidina, A.G., 2013. A new conceptual model of the Icelandic crust in the Hengill geothermal area based on the indirect electromagnetic geothermometry, *J. Volc. Geotherm. Res.,* **257,** 99–112.

Spratt, J.E., Jones, A.G., Jackson, V.A., Collins, L. & Avdeeva, A., 2009. Lithospheric geometry of the Wopmay orogen from a Slave craton to Bear Province magnetotelluric transect, *J. geophys. Res.,* **114,** B01101, doi:10.1029/2007JB005326.

Stegena, I., 1976. Electric conductivity structure and geothermal reservoirs, *Acta Geodaet., Geophys. et Montanist. Acad. Sci. Hung. Tomus,* **11**(3–4), 377–397.

Sternberg, B.K., 1993. On: "Removal of static shift in two dimensions by regularized inversion" by Catherine deGroot-Hedlin, *Geophysics,* **58,** 598–599.

Sternberg, B.K., Washburne, J.C. & Pellerin, L., 1988. Correction for the static shift in magnetotellurics using transient electromagnetic soundings, *Geophysics,* **53**(11), 1459–1468.

Strachan, S., 2001. A Geophysical Investigation of the Eyjafjallajökull Glaciovolcanic System, South Iceland, using radio echo sounding, *PhD thesis,* University of Edinburgh.

Sturkell, E., Sigmundsson, F. & Einarsson, P., 2003. Recent unrest and magma movements at Eyjafjallajökull and Katla volcanoes, Iceland, *J. geophys. Res.,* **108,** 2369, doi:10.1029/2001JB000917.

Sturkell, E., Einarsson, P., Sigmundsson, F., Hooper, A., Ófeigsson, B.G., Geirsson, H. & Ólafsson, H., 2010. Katla and Eyjafjallajökull Volcanoes, *Dev. Quater. Sci.,* **13**.

Tarasewicz, J., Brandsdóttir, B., White, R.S., Hensch, M. & Thorbjarnardóttir, B., 2012a. Using microearthquakes to track repeated magma intrusions beneath the Eyjafjallajökull stratovolcano, Iceland, *J. geophys. Res.,* **117,** B00C06, doi:10.1029/2011JB008751.

Tarasewicz, J., White, R.S., Woods, A.W., Brandsdóttir, B. & Gudmundsson, M.T., 2012b. Magma mobilization by downward-propagation decompression of the Eyjafjallajökull volcanic plumbing system, *Geophys. Res. Lett.,* **39,** L19309, doi:10.1029/2012GL053518.

ten Grotenhuis, S.M., Drury, M.R., Spiers, C.J. & Peach, C.J., 2005. Melt distribution in olivine rocks based on electrical conductivity measurements, *J. geophys. Res.: Solid Earth,* **110,** B12201, doi:10.1029/2004JB003462.

Utada, H., Takahashi, Y., Morita, Y., Koyama, T. & Kagiyama, T., 2007. ACTIVE sytsem for monitoring volcanic activity: a case study of the Izu-Oshima Volcano, Central Japan, *J. Volc. Geotherm. Res.,* **164**(4), 217–243.

Watanabe, H., Yamashita, H. & Maekawa, T., 1984. Electrical study of the 1977–1982 actvitiy of Usu volcano, *Geophys. Bull. Hokkaido Univ.,* **43,** 31–40.

Weir, N.R.W., White, R.S., Brandsdóttir, B., Einarsson, P., Shimamura, H. & Shiobara, H. The RISE Fieldwork Team, 2001. Crustal structure of the northern Reykjanes Ridge and Reykjanes Peninsula, southwestern Iceland, *J. geophys. Res.,* **106,** 6347–6368.

White, R.S. *et al.*, 1996. Seismic images of the crust beneath Iceland contribute to long-standing debate, *EOS, Trans. Am. geophys. Un.,* **77**(21), 197–201.

Wiese, H., 1962. Geomagnetische Tiefentellurik. II. Die Streichrichtung der Untergrundstrukturen des elektrischen Widerstandes, erschlossen aus geomagnetischen Variationen, *Geofis. Pura Appl.,* **52,** 83–103 (in German).